Microscopy and Microanalysis, 2026, **32**, ozaf118
https://doi.org/10.1093/mam/ozaf118
Advance access publication 12 January 2026
Original Article

Microscopy AND Microanalysis

Trimetazidine Attenuates Ulcerative Colitis-Linked Extrapyramidal Dysfunction by Mediated Dectin-1/LRRK2/α-Synuclein Autophagy Axis

Shaimaa H. Mahmoud[1], Sameeah Mejbel Hamad Algenabi[2], Anwar Nather Seiwan[3], Dalia Alaa El-Din Aly El-Waseef[4], Omnyah A. El-Kharashi[1,5], Asmaa M. Elshaer[1], Emad R. Sindi[6], Tahani Mohamed Ibrahim Al-Hazani[7], Samar F. Ezzat[4], Ahmed Essmat[8], Hyfa A. Alzahrani[9], Fawzyah Obeedallah Albaldi[9], Amal F. Dawood[10], Hebatallah H. Abo Nahas[11,*], and Doaa I. Mohamed[1]

[1]*Department of Clinical Pharmacology and Therapeutics, Faculty of Medicine, Ain Shams University, Cairo 11591, Egypt*
[2]*Department of Human Anatomy, College of Medicine, University of Anbar, Anbar, Ramadi City 55431, Iraq*
[3]*Department of Biology, College of Science, University of Basrah, Basrah 61004, Iraq*
[4]*Department of Histology and Cell Biology, Faculty of Medicine, Ain Shams University, Cairo 11591, Egypt*
[5]*Department of Clinical Pharmacology and Therapeutics, Faculty of Medicine, Misr University for Science and Technology, Cairo 77, Egypt*
[6]*Department of Basic Medical Sciences, College of Medicine, University of Jeddah, Jeddah 23890, Saudi Arabia*
[7]*Biology Department, College of Science and Humanities, Prince Sattam bin Abdulaziz University, Al-Kharj 16273, Saudi Arabia*
[8]*Department of Neurology, Faculty of Medicine, Al Azhar University, Cairo 11651, Egypt*
[9]*Department of Biology Faculty of Science, Al-Baha University, Alaqiq 65779-7738, Saudi Arabia*
[10]*Department of Basic Medical Sciences, College of Medicine, Princess Nourah bint Abdulrahman University, P.O. Box 84428, Riyadh 11671, Saudi Arabia*
[11]*Physiology Biochemistry Division Zoology Department, Faculty of Science, Port Said University, Port Said 42511, Egypt*

***Corresponding author:** Hebatallah H. Abo Nahas, E-mail: heba.hassan@sci.psu.edu.eg

This research was performed at the Faculty of Medicine, Ain Shams University, Cairo, Egypt

Abstract

Chronic relapsing colonic inflammation, specifically ulcerative colitis (UC), causes persistent mucosal injury and disrupts the gut–brain axis. This disruption leads to basal ganglia neuroinflammation and ultimately extrapyramidal motor dysfunction. Dysregulation of the Dectin 1/leucine-rich repeat kinase 2 (LRRK2)/α-synuclein (αSyn) signaling exacerbates inflammation. This study investigated whether modulation of this pathway affects UC progression and is associated with motor deficits using trimetazidine (TMZ) treatment in a Bagg albino c (BALB/c) mice model. Furthermore, we examined the role of this pathway through molecular docking followed by molecular dynamics simulations to evaluate the plausibility of TMZ interactions with Dectin-1, LRRK2, and α-syn proteins. Our results indicate that TMZ improved behavioral changes and also significantly reduced serum interferone-γ (IFN-γ) and NF-kB levels, along with decreased Dectin-1, LRRK2, and αSyn expression. TMZ also mitigated colonic inflammation, as shown by reducing fecal calprotectin and fecal occult blood, supported by histological examinations. Furthermore, TMZ restored autophagic flux by reducing P62 accumulation and enhancing LAMP2 expression. Molecular docking and dynamics confirmed TMZ binding to Dectin-1, LRRK2, and αSyn, through hydrophobic and hydrophilic interactions. These findings suggest a potential molecular basis for the observed associations between the Dectin-1/LRRK2/α-synuclein axis and UC-related motor dysfunction, warranting further experimental validation, establishing TMZ's therapeutic potential for managing colonic inflammation and associated neurological manifestations.

Key words: αSyn, autophagy, dectin 1, LRRK2, motor dysfunction, TMZ, ulcerative colitis

Received: March 4, 2025. **Revised:** September 24, 2025. **Accepted:** November 14, 2025

Graphical abstract

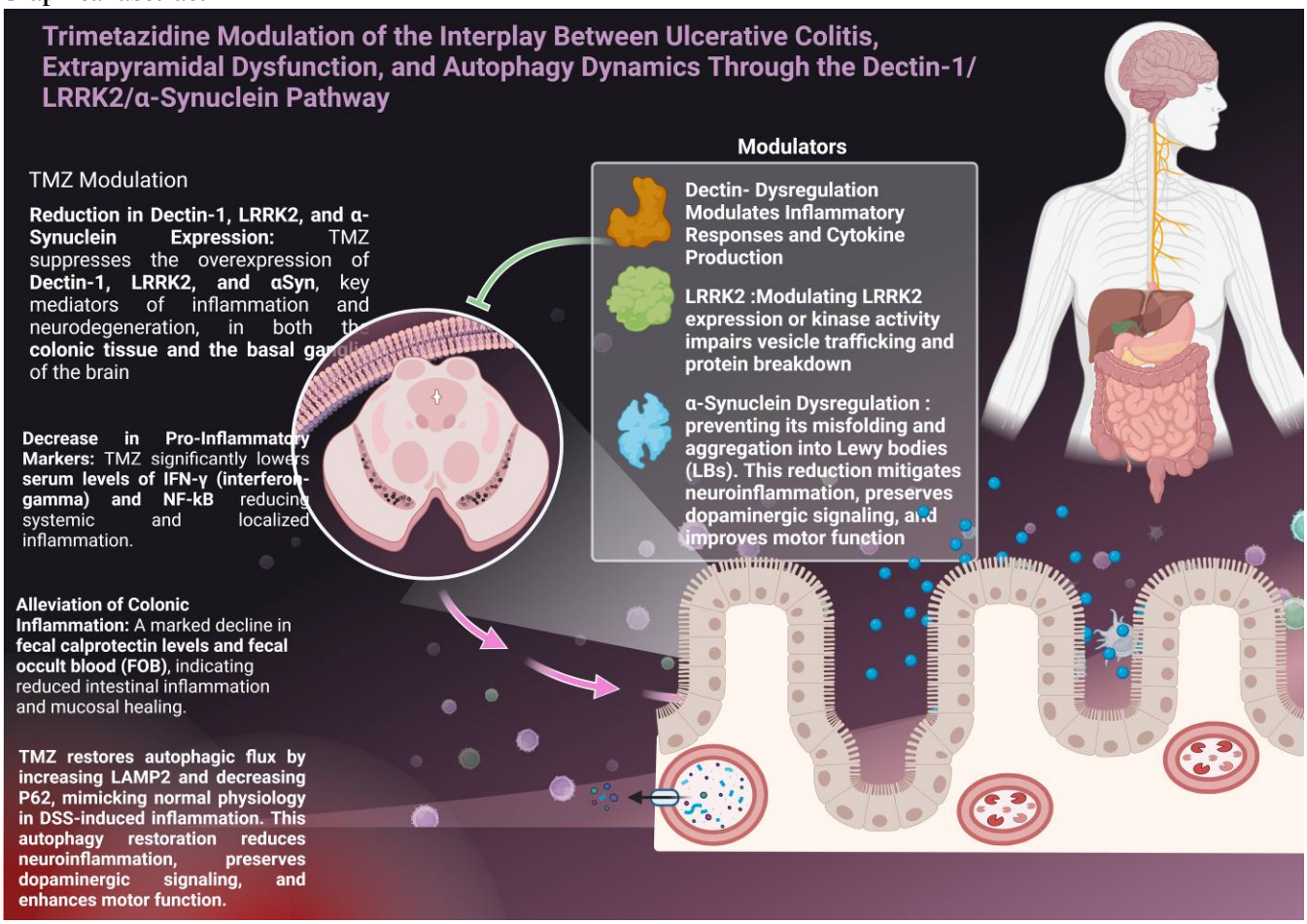

Introduction

Ulcerative colitis (UC) is a lifelong idiopathic inflammatory bowel disease characterized by relapsing and remitting mucosal inflammation that extends from the rectum to the proximal colon (Kaur & Goggolidou, 2020). Beyond the gastrointestinal system, UC is demonstrated to have systemic impacts, particularly through the brain–gut axis, which has been increasingly linked to neurodegenerative conditions (Günther et al., 2021). The global incidence of UC has been reported to range from 1.2 to 20.3 cases to 7.6 to 245 cases per 100,000 persons per year, respectively (Gajendran et al., 2019). Numerous pharmaceutical agents are currently employed in the treatment of UC; however, the development of new, efficient, and promising treatments is imperative due to the identified negative consequences (Kayal & Shah, 2020). Recent findings indicate a correlation between UC and neurodegenerative diseases, such as Parkinson's disease (PD) (Kornelsen et al., 2021; AboNahas et al., 2022).

The presence of pathological changes in the enteric nervous system has been observed to extend along the length of the vagus nerve. This phenomenon induces neuroinflammation and potentially contributes to motor dysfunction development (Safarpour et al., 2022). Additionally, intestinal inflammation induced by various gastrointestinal disturbances has been shown to exacerbate peripheral inflammation (Mohamed et al., 2022, 2023), which may propagate neuroinflammation and motor dysfunction-associated neuropathology (Warnecke et al., 2022). Dectin-1 (Dendritic Cell-Associated C-Type Lectin-1), a pattern recognition receptor primarily expressed in dendritic cells, and its stimulation drives the NF-κB inflammatory cascade, characterized by elevated cytokines, impaired autophagic flux, and subsequent disturbance in cellular homeostasis (Takagawa et al., 2018). Prolonged immune response elevates cytokine Interferon-γ IFN-γ, resulting in extensive leukocyte infiltration and mucosal injury (Langer et al., 2019). Remarkably, IFN-γ has been observed to target the leucine-rich repeat kinase 2 (LRRK2) gene, resulting in augmentation in NF-κB transcription (Panagiotakopoulou et al., 2020).

Dextran sulfate sodium (DSS)-colitis models introduce a robust gut–brain axis evaluation, reliably inducing extrapyramidal motor dysfunction that reflects Parkinsonian pathology (Villarán et al., 2010). PD is marked by the degeneration of dopaminergic neurons in the substantia nigra pars compacta (SNc), and diminished dopamine levels in the striatum (Lang & Lozano, 1998). O'Hara et al. reported that the activation of NF-κB by LRRK2 is recognized to contribute to autophagy dysfunction, impairing the clearance of misfolded or superfluous proteins. This dysfunction leads to the formation of Lewy bodies (LB) protein clumps, resembling those observed in patients with sporadic PD (O'Hara et al., 2020). The basic disease markers of PD encompass the death of

dopamine-producing neurons in the SNc and the buildup of α-synuclein (*α*Syn) into large clumps (LB), which predominantly contain phosphorylated *α*Syn, ubiquitin, p62, and malformed lipid membranes and organelles (Chartier & Duyckaerts, 2018; Shahmoradian et al., 2019). One of the most widely studied autophagy receptors, p62 (SQSTM-1), functions as an autophagy substrate, and its levels are correlated with autophagy activity (Moscat & Diaz-Meco, 2009).

P62, an adaptor protein, functions as the recognition receptor for the degradation of ubiquitinated proteins and organelles (Johansen & Lamark, 2011). As a selective cargo receptor, it facilitates clearance of misfolded proteins by transporting polyubiquitinated proteins to autophagosomes for proteasomal degradation. Due to its critical role, it has garnered increased attention in diseases such as PD (Liu et al., 2017). Additionally, lysosome-associated membrane protein 2 (LAMP-2) is widely used as a marker for autophagolysosomes and lysosomes and is essential for autophagosome–lysosome fusion (Huynh et al., 2007). In murine models, the genetic manipulation of the LAMP-2A gene, which encodes a predominant LAMP-2 isoform, has been demonstrated to enhance the diminished levels of autophagy and chaperone-mediated autophagy in aged hepatic cells (Zhang & Cuervo, 2008).

Trimetazidine (TMZ) is a cutting-edge anti-ischemic medication that safeguards cells during hypoxic conditions (Alzahrani et al., 2024). It is demonstrated to alleviate angina episodes and symptoms in patients unresponsive to therapeutic interventions by restricting the production of oxidative damage (Glezer et al., 2018). TMZ, a piperazine-based compound, is a pioneering agent in a new class of metabolic agents. It exerts cytoprotective impact on the heart and other vital organs by reducing reactive oxygen species damage and enhancing blood capillary function (Dézsi, 2016; Luo et al., 2021). TMZ confers its beneficial effects through mediating oxidative stress from inflammation (Abdel-Salam et al., 2011), likely through inhibition of NF-kB and the subsequent downstream inflammatory mediators (Alzahrani et al., 2024). Numerous studies have investigated alterations in brain structure and function in UC. From this concept, the objective of our study is to investigate a new pathway of extrapyramidal dysfunction of BALB/c mice model in UC and validate the role of the Dectin-1/LRRK/*α*Syn-linked autophagy pathway in connecting UC to PD. Furthermore, we explored the pharmacological potential of TMZ modulation in extrapyramidal dysfunction-associated UC by addressing autophagic dysfunction through Dectin-1/LRRK2/*α*Syn axis modulation.

Materials and Methods

Study Design

This study investigated the role of Dectin-1, LRRK2, and α-synuclein, as well as autophagy dynamics in UC and extrapyramidal dysfunction in BALB/c mice. The research was conducted in the Department of Pharmacology and the Medical Research Center, Faculty of Medicine, Ain Shams University, Cairo, Egypt. The research adhered to ethical standards (FWA000017585). Over a four-month investigation allowed for UC induction, therapeutic drug administration, and assessment of behavioral, biochemical, and histological parameters; all procedures were approved by the Institutional Animal Ethics Committee of Ain Shams University (FMASUMD 99-2022). Forty-five male BALB/c mice (6–8 weeks old, 20–30 g), sourced from the Odor Bilharz Research Institute in Giza, Egypt, were housed under standard laboratory conditions and divided into three groups of fifteen. Mice that died early during DSS treatment or were otherwise unwell due to unrelated causes were excluded, after accounting for natural mortality (40%, primarily during initial UC induction). 8 mice per group were studied. The Control Group received a standard diet and water (Li et al., 2021*a*); the DSS Group underwent five cycles of UC induction using 3% DSS in drinking water for 7 days, followed by 10 days of distilled water (Okayasu et al., 1990). The TMZ Treatment Group received oral Trimetazidine (20 mg/kg/day) for four weeks after 12 weeks of DSS-induced UC (El-Sherbeeny & Attia, 2016).

Study Materials

Drugs and Chemicals: DSS (Sigma), TMZ (Sigma), and formaldehyde are used for the histological processing of tissues.

- DSS, dextran sulfate sodium, is supplied by Sigma-Chemical Co., Cairo, Egypt, as a white to off-white powder dissolved in distilled water for oral administration. Its molecular formula is ($C_6H_7Na_3O_{14}S_3$).
- 1-(2,3,4-Ttrimethoxybenzyl) piperazine (MW = 266.34) is a white, odorless powder dissolved in distilled water for oral administration. Its molecular formula is ($C_{14}H_{22}N_2O_3$).
- Neutral-buffered formaldehyde solution (10%) was procured from El Gomhoreya Chemicals Company, Egypt. It is used as a fixative solution for histological preparation.

Diet: Standard pellets contain 20% protein, 10% fat, and 70% carbohydrates. They are produced by Meladco for Animal Food, Egypt.

Equipment: The Open Field Test apparatus, Rotarod, was used for behavioral assays.

Methodological Steps

BALB/c mice were acclimated for one week under controlled conditions (12/12-h light/dark cycle, 25°C). The animals were housed in cages containing three animals each. UC was induced in DSS and TMZ groups using DSS-treated water. After 12 weeks of DSS cycles, a TMZ was administered to the TMZ group. The primary outcome measures included behavior, biochemical, and molecular biomarkers.

Determination of Behavioral Profile in DSS-Induced UC in BALB/c Mice

In order to gain insight into the effects of TMZ on the modulation of behavior profiles and determine the subsequent effects of TMZ on motor coordination, balance, and strength, the Open Field Test (OFT) and Rotarod Test were employed according to (Seibenhener & Wooten, 2015; Abuelezz et al., 2017; Habib et al., 2022). Behavioral evaluations were conducted before and after the treatment, assessing motor coordination, functional balance, and anxiety levels.

Open Field Test

The OFT is applied to evaluate movements in a defined arena, anxiety-related behaviors, and exploratory tendencies. Mice were transported in their designated cages to the experimental

testing facility and allowed to acclimate for 30 min before testing. The mouse was gently grasped by its tail and situated at the core of the open field maze. The mouse instinctively moves toward the peripheral boundaries of the maze, and release and motion tracking were synchronized to accurate behavioral recording. The subject mouse was gently retrieved, removed from the maze, and returned to its cage after 10 min of unrestricted and continuous movement in the specified quadrant. The fecal boli pellets were enumerated and analyzed prior to the sanitation of the maze (Seibenhener & Wooten, 2015). Within OFT, each mouse was individually positioned at the center of a quadrangular arena measuring 60×60 cm with walls 45 cm in height. The arena was subdivided into 16 equal squares, each illuminated by white light, and each mouse underwent testing for 5 min. The testing process was documented via a webcam. The parameters recorded during the 5-min observation period included (1) the number of crossed squares (defined as visiting with all four feet within a single square), (2) the number of entries into the central zone (comprising the central four squares), (3) the latency to exit the central zone and the duration spent within it, and (4) the frequency of both rearing (standing upright on the hind limbs) and grooming (comprising face rubbing and the licking or biting of both paws and fur (Abuelezz et al., 2017).

Rotarod Test

The rotarod test assessed motor skills and the general behavior profile. The average duration of each mouse on the rodent cylindrical structure was used to indicate muscular development. Mice were evaluated for motor coordination by being positioned individually on a rotarod apparatus (6-cm rotor diameter operating at a constant velocity of 20 rpm). Mice underwent a training regimen to sustain their posture on the rotarod across three distinct training sessions, each lasting 5 min, prior to the commencement of the therapeutic intervention. On the tenth day of the study, mice performed three consecutive rotarod trials with a maximum duration of 180 s per trial, separated by 5-min rest intervals to assess motor coordination. The duration of falls was determined by calculating the mean of the falling times recorded across the three trials (Habib et al., 2022).

Determination of Weight Changes in DSS-Induced UC in BALB/c Mice

Body weight was carefully monitored at the following time points: before starting each DSS cycle, after completing the final cycle, and following any weight changes observed after TMZ administration.

Determination of the Inflammatory Modulation Profile in DSS-Induced UC in BALB/c Mice

Inflammatory responses were assessed at both systemic and local levels; systemic markers (serum IFN-γ and NF-κB levels) and local intestinal markers (fecal calprotectin and occult blood) were measured. Blood samples were obtained from cardiac puncture and centrifuged for 15 min at 3,000 rpm; serum samples were preserved at −80°C. Serum IFN-γ (minimum detectable concentration: 9.38 pg/mL; R&D Systems, Cat. No. 485-M, MN, USA) and NF-κB (minimum detectable concentration: 0.19 ng/mL; Biorbyt, Cat. No. orb866940, Cambridge, UK) levels were measured using a microplate reader (BioTek, Winooski, VT, USA) according to manufacturer's guidelines at 450 ± 2 nm. Serum samples were diluted 1:2 in assay buffer prior to processing with specific detection antibodies and streptavidin–Horseradish Peroxidase (HRP) conjugate. Samples were collected in sterile containers and homogenized in an extraction buffer containing protease inhibitors to analyze fecal inflammatory markers. Calprotectin (sensitivity: 1.88 ng/mL; Elabscience, Cat. No. E-EL-M1143, Wuhan, China) and fecal occult blood (FOB; sensitivity: 100 ng/mL; MyBioSource, Cat. No. MBS318861, California, USA) were measured as intestinal inflammation markers using theenzyme-linked immunosorbent assay (ELISA) sandwich method. The fecal homogenates were vortexed, and the supernatant was mixed with a test diluent. Following phosphate-buffered saline (PBS)–Tween buffer washes, samples were incubated with biotinylated detection antibody and streptavidin–HRP conjugate. Color development was initiated with 3,3',5,5'-tetramethylbenzidine (TMB) substrate, terminated with HCl, and optical density was measured at 450 ± 2 nm.

Determination of the Dectin-1, LRRK2, and α-Syn Profile in DSS-Induced UC in BALB/c Mice

The amounts of Dectin-1, LRRK2, and α-Syn were quantified in colonic and brain tissues via quantitative reverse transcription polymerase chain reaction (qRT-PCR). (Table 1) lists primer pairs used in qRT-PCR analysis for the selected genes (Table 1). The isolation of RNA from BALB/c mice was conducted utilizing the RNeasy Mini Kit (Qiagen, Hilden, Germany), in accordance with the manufacturer's protocol. The purity and concentration of RNA were evaluated using a NanoDrop 1000 spectrophotometer (Thermo Fisher Scientific, USA), with samples exhibiting an A260/A280 ratio ranging from 1.8 to 2.1. Following the manufacturer's instructions, the reverse transcription process was conducted using MiScript II RT PCR kits (Qiagen catalogue no. 218161, Hilden, Germany). The reverse transcription mixes were preserved at a temperature of −20°C before the execution of real-time PCR. A reaction mix for qPCR was formulated with 10 μL of 2× RT2 SYBR Green ROX qPCR Master Mix (Qiagen), specific primers for Dectin-1, LRRK2, and α-Synuclein, 2 μL of template cDNA, and RNase-free water to achieve a total volume of 20 μL—the (The β-actin, NM_001101) gene was utilized as the housekeeping gene for normalization purposes. Reactions were conducted on a Rotor-Gene real-time PCR detection system (Qiagen) under the following parameters: initial denaturation at 95°C for 10 min, followed by 45 cycles comprising denaturation at

Table 1. The List of Primer Pairs Used in qRT-PCR Analysis for the Selected Genes.

Gene Name	Forward Primer	Reverse Primers
Dectin-1	TAGTAGTGGTTGCTGCAGTGCTG	GATAGGAAGTTGTCTTTCTCCTCTGG
α-synuclein	TGACAGCAGTCGCTCAGA	CATGTCTTCCAGGATTCCTTC
LRRK2	GCCACGAATCTCAATAGCAAG	CCAAGCCAAGCACAGATTC

95°C for 15 s, annealing at 55°C for 30 s, and extension for 30 s. A melting curve analysis (55–95°C) was conducted to confirm amplicon specificity. The melting curve was examined to verify the specificity of the amplicons for qPCR. The relative expression of target genes was calculated using the 2−ΔΔCT (Cycle threshold) formula.

Determination of Autophagy-Related Biomarkers Profile in DSS-Induced UC in BALB/c Mice

The LAMP-2 and p62 expression levels were analyzed in colonic and brain tissue homogenates using immunoblotting. Tissue samples were processed with the ReadyPrep™ Protein Extraction Kit (Bio-Rad, #163-2086), with 20 μg protein mixed with 2× Laemmli buffer (Bio Basic Inc., #SK3041) containing 4% Sodium Dodecyl Sulfate (SDS), 20% glycerol, 10% 2-mercaptoethanol, 0.004% bromophenol blue, and 0.125 M Tris-HCl (pH 6.8). After denaturation (95°C, 5 min), proteins were separated on Tris-Glycine eXtended (TGX) Stain-Free™ gels (Bio-Rad, #161-0181) and transferred to polyvinylidene fluoride (PVDF) membranes using the Trans-Blot Turbo system (25 V, 7 min).

Membranes were blocked in TBST (Tris-Buffered Saline with Tween 20) containing 3% BSA (Bovine Serum Albumin) before incubation with primary antibodies: anti-LAMP2 (Creative Biolabs, #GPX04-147J), anti-p62 (Cell Signaling, #88588), and anti-β-actin (loading control) in TBST (24 h, 4°C). After washing, membranes were incubated with HRP-conjugated secondary antibodies, and proteins were detected using Clarity™ Western ECL Substrate (Bio-Rad, #170-5060). Band intensities were quantified using the ChemiDoc MP system and normalized to β-actin.

Histopathological Studies

All animals were anesthetized using thiopental sodium (intraperitoneal). The brain and colon of each mouse were taken. The colon was opened longitudinally and washed properly with saline to remove food remnants and mucous. Brain and Colon specimens were rapidly fixed in 10% neutral-buffered formalin, dehydrated, and cleared to obtain paraffin blocks. Sections of both organs were cut at a 5-μm thickness and prepared for:

- Naked eye appearance.
- Light microscopic examination with hematoxylin–eosin (H&E) stain for colon and brain.
- Mallory's trichrome stain for colon collagen.
- Immunohistochemistry study for the brain.

Microscopic inflammation and tissue morphology were evaluated using an Olympus CKX41 light microscope (Olympus Corporation, Tokyo, Japan). The mucosal integrity and collagen fiber deposition were specifically assessed in colon samples.

Immunohistochemical Study for Detection of Tyrosine Hydroxylase Antibody and αSyn

To detect cerebral tissue changes, we employed an immunohistochemical method utilizing an avidin–biotin–peroxidase technique to evaluate anti-TH antibody (to show the distribution of dopaminergic neurons in the substantia nigra), and anti-α-synuclein (to detect the protein α-synuclein) (Lab Vision, CA, USA), in accordance with the manufacturer's protocol. Initially, we treated deparaffinized and retrieved tissue sections with 0.3% hydrogen peroxide for 20 min. Brain samples were then incubated overnight at 4°C with an anti-TH antibody (ab112, Abcam) at a 1:200 dilution and an anti-α-synuclein antibody (32-8100, Thermo Fisher) at a 1:100 dilution. The reaction was visualized through development with 3,3'-Diaminobenzidine (DAB) solution (DAKO, Denmark) for 10 min, followed by counterstaining with Mayer's hematoxylin. The slides were dehydrated, cleared with xylene, and cover-slipped for microscopic examination.

Morphometric Study

For quantitative metrics, the ImageJ program (version 1.2.2006) was utilized for a morphometric study to measure several parameters from colonic and cerebral tissues. Specifically, the diameter and mucosal thickness of the colon were measured using (4× lens power) and the area percentage of collagen fibers using a (40× lens power) from H&E- and Mallory's trichrome-stained sections, respectively. From the cerebral tissues, we counted the number of nerve cells positive for tyrosine hydroxylase (TH), denoting the dopaminergic neurons in the substantia nigra, and the number of neurons positive for anti-α-synuclein, both using a (40× lens power). We analyzed five different non-overlapping fields for each parameter from five specimens obtained from all mice.

In Silico Molecular Docking Study

Molecular docking simulations were conducted using AutoDock 4.2 to explore the potential binding orientations and affinities of TMZ with Dectin-1, LRRK2, and α-synuclein.(Santos-Martins et al., 2014). To validate the docking protocol, three reference ligands were employed: Laminarin, a β-1,3-glucan (Xie et al., 2010) known to bind the carbohydrate-recognition domain of Dectin-1; the co-crystallized kinase inhibitor LRRK2-IN-1 from PDB ID: 4YZM; and epigallocatechin gallate (EGCG) (Xu et al., 2016), a polyphenol from green tea, is reported to inhibit α-synuclein aggregation. These control ligands were used as benchmarks to ensure the reliability and specificity of the docking results for TMZ.

The 3D structures of TMZ, Laminarin, and EGCG were obtained from the PubChem database, followed by energy minimization using the MMFF94 force field in Avogadro. The LRRK2-IN-1 inhibitor was extracted directly from the 4YZM crystal structure. Ligands were prepared by adding Gasteiger charges, defining torsional degrees of freedom, and converting them to PDBQT format using AutoDockTools (ADT). For the protein receptors, the X-ray crystal structures of Dectin-1 (PDB ID: 2BPH), LRRK2 (PDB ID: 4YZM), and α-synuclein fibril (PDB ID: 6A6B) were retrieved from the Protein Data Bank. All non-essential heteroatoms, ions, and water molecules were removed, while polar hydrogens and Kollman charges were added. The processed receptors were also converted into PDBQT format via ADT.

The docking grids were defined to encompass each target's known or predicted binding regions. Dectin-1's grid box was centered on the carbohydrate-recognition domain, as determined from Laminarin docking and structural data. For LRRK2, the grid was centered on the Adeonsine triphosphate (ATP)-binding site where LRRK2-IN-1 is co-crystallized, ensuring accurate targeting of the active site. For α-synuclein, which lacks a conventional binding pocket, potential ligandable cavities were predicted using computed atlas of surface topology of proteins (CASTp), and the grid box was centered on the most prominent surface cavity where EGCG is known

to interact. Each grid box was set with dimensions of 60 × 60 × 60 Å and a grid spacing of 0.375 Å.

Docking simulations were performed using the Lamarckian Genetic Algorithm (LGA) (Morris et al., 1998) with 100 independent runs per ligand. The algorithm parameters included a population size of 150, a maximum of 2,500,000 energy evaluations, and 27,000 generations. The resulting poses were ranked based on predicted binding free energy (ΔG). The top-ranked poses from each cluster were selected for further analysis. To validate the docking protocol, each reference ligand was first docked into its respective protein target. Laminarin docking into Dectin-1 confirmed the carbohydrate-binding groove predicted by structural studies, while re-docking of LRRK2-IN-1 into LRRK2 reproduced the co-crystallized conformation with minimal root mean square deviation (RMSD) deviation, confirming the accuracy of the docking grid and scoring function. EGCG docking into α-synuclein validated the predicted binding cavity and provided a comparative reference for evaluating the binding affinity of TMZ. All docking results were analyzed using AutoDockTools and visualized with Discovery Studio Visualizer (Jejurikar & Rohane, 2021).

Molecular Dynamics Simulations

To evaluate the stability and dynamic behavior of the TMZ complexes with Dectin-1, LRRK2, and α-synuclein, molecular dynamics (MD) simulations were performed for 100 ns using GROMACS 2023.2 (Van Der Spoel et al., 2005). The initial protein–ligand complexes were obtained from the lowest-energy docking poses for each target.

The protein structures of Dectin-1 (PDB ID: 2BPH), LRRK2 (PDB ID: 4YZM), and α-synuclein fibril (PDB ID: 6A6B) were pre-processed using the pdb2gmx module of GROMACS. The CHARMM36 m force field was employed for protein parameterization (Huang et al., 2017). The ligand TMZ was parameterized using the CGenFF server (ParamChem) to generate topology and parameter files compatible with the CHARMM force field (Vanommeslaeghe et al., 2010). The complexes were then placed in a dodecahedral unit cell shape simulation box with at least a 10 Å distance between the protein surface and the box edge, ensuring sufficient space for solvent and periodic boundary conditions.

The simulation box was solvated using the TIP3P water model, and the system was neutralized by adding counterions (Na^+ or Cl^-) using the genion tool. To mimic physiological ionic strength, 0.15 M NaCl was added.

Energy minimization was performed using the steepest descent algorithm until the maximum force reached <1,000 $kJ{\cdot}mol^{-1}{\cdot}nm^{-1}$. Following minimization, the system underwent two equilibration phases: NVT (constant Number of particles, Volume, and Temperature) equilibration for 500 ps at 310 K, with position restraints on heavy atoms, using the V-rescale thermostat, and NPT (constant Number of particles, Pressure, and Temperature) equilibration for 500 ps at 1 bar using the Parrinello–Rahman barostat.

The production MD simulations were conducted for 100 ns without restraints, employing a time step of 2 fs. Long-range electrostatics were handled using the Particle Mesh Ewald (PME) method with a cutoff of 10 Å for Coulomb and van der Waals interactions. The LINCS algorithm was applied to constrain all hydrogen-containing bonds.

Post-simulation analyses were carried out to assess structural stability and protein–ligand interactions. Also, interaction fraction plots were generated to identify dominant contacts between TMZ and active site residues. Binding free energy estimations were performed using the muscularis mucosa (MM)-PBSA method via the g mmpbsa package.

Sample Size and Statistical Analysis

The sample size was determined using Graph Pad Stat Mate (Version 1.01), calculated based on a two-tailed study with a power of 80%, a significance level of 0.05, and an expected effect size. The minimum number of animals required for each group was six. The data were analyzed using SPSS (Version 20); the number of subjects in each group was determined based on the anticipated effect size and standard deviation. Thus, it was ensured that the study could detect significant effects on the hypotheses across the remaining experimental outcome measures. Considering the groups' differences, behavioral, biochemical, molecular, and histological data were subject to statistical comparison analysis. Power analysis was performed for the following levels: p-values less than 0.05, 0.01, and 0.001 were considered statistically significant. The correlation between brain αSyn and fecal calprotectin was analyzed using a linear regression curve (Fig. 1).

Results

TMZ Ameliorates Extrapyramidal Motor Dysfunction Associated With DSS-induced UC- BALB/c Mice

Open Field Test

We employed the OFT to provide a detailed picture of stereotyped behaviors and TMZ's modulation in DSS-induced UC-BALB/c mice. Our result revealed a significant behavioral alteration following 3% DSS administration, including a substantial decline in the total number of crossed squares, indicating a reduction in locomotor activity. This suggests that the mice are less active, which is likely due to DSS administration. Additionally, the reduction in entry numbers to the central zone and rearing frequency ($p < 0.0001$) further indicates reduced exploratory behavior and increased anxiety. Moreover, a significant increase in the duration spent in the central zone and the latency to leave the central zone, indicating "freezing behavior" ($p < 0.0001$). The observed increase in the frequency of grooming ($p < 0.0001$) in the DSS group compared to the control group suggests that these mice may be experiencing higher levels of stress or anxiety, which could be contributing to an increased propensity for grooming as a coping mechanism. Interestingly, the TMZ-administered group demonstrates a substantial elevation in the total number of crossed squares ($p < 0.05$), entries to the central zone ($p < 0.001$), and rearing frequency ($p < 0.0001$). These findings suggest that TMZ administration effectively recovers locomotor activity and exploratory behavior. The TMZ-treated group exhibited a decline in grooming frequency compared to the DSS group ($p < 0.0001$), indicating reduced stress and anxiety levels. This suggests that the neuroprotective impact of TMZ administration, which effectively minimizes the behavioral impairments caused by DSS, may restore the behavior of the treated mice to its baseline levels (Fig. 2).

Rotarod Test

To evaluate the effects of TMZ on motor activity in DSS-induced UC in BALB/c mice model, motor coordination,

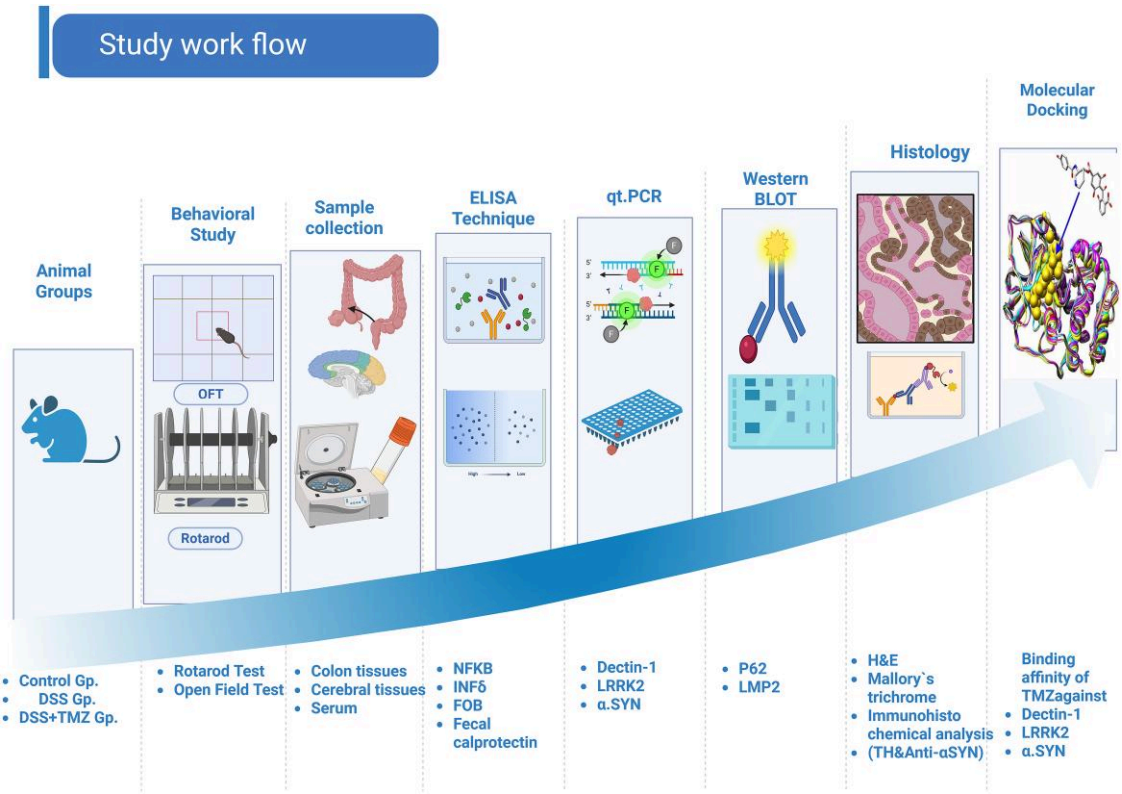

Fig. 1. The proposed approach seeks to clarify the molecular interactions among Dectin-1, LRRK2, and the α-Syn axis in influencing UC, as well as the possible protective effects of TMZ. The workflow delineates the subsequent essential steps: Identification of target interactions by experimental validation, functional tests to evaluate the effects on cellular processes pertinent to UC, and a thorough study of gene expression alterations in colonic and brain tissue samples to elucidate the regulatory mechanisms involved. Histological and immunochemical evaluations to analyze the structural architecture of colonic and brain tissues.

strength, and balance were assessed using the rotarod test. Subject mice were mounted on a rotating rod, and the duration of upright steadiness without falling in any direction was recorded. Our results showed that the motor coordination and balance of DSS-induced UC in the BALB/c mice group decreased over time due to the administration of 3% DSS. A significant difference was identified between the DSS group and the control group ($p < 0.0001$). This finding suggests a potential negative impact of 3%DSS-induced UC on motor functions. The observed decline in motor coordination suggests that UC may have extrapyramidal effects that affect motor control. Interestingly, the administration of TMZ in DSS-induced BALB/c mice for 4 weeks resulted in a significant ($p < 0.0001$) improvement in motor function. As shown in Fig. 3, a small difference was observed between the TMZ group and the control group. Furthermore, a significant difference ($p < 0.0001$) was found between the DSS and TMZ groups. Underscoring the potential therapeutic effect of TMZ in ameliorating motor shortages, the statistical analysis supports the conclusion that TMZ's neuroprotective properties may contribute to its effectiveness in mitigating UC-related motor deficiencies.

TMZ Treatment Enhanced Weight Changes Associated With DSS-Induced UC-BALB/c Mice

The temporal administration of TMZ treatment is critical in evaluating its influence on variations in body weight associated with DSS-induced UC in BALB/c mice. Consequently, the substantial interaction effect between the temporal factors (cycles and treatment) and TMZ administration underscores the concept that the influence of these agents on the body weight of the subjects fluctuates across various temporal intervals. The 3% DSS-induced UC mice group revealed a notable reduction in body weight ($p < 0.0001$). This result is consistent with the anticipated response to DSS administration, which induces inflammatory responses and simulates UC's physiological symptoms, leading to weight loss. In contrast, the TMZ administration group, which received TMZ at a dosage of 20 mg/kg/day for 4 weeks, showed a statistically significant difference in body weight relative to the control and the DSS administration groups. The graphical representation clearly represents the partial restoration seen in the TMZ-treated group, and the differences among all groups (Fig. 4). This evidence suggests that TMZ may exhibit therapeutic efficacy, illustrating its ability to attenuate DSS-induced weight loss over time. The different delineation of bars or markers highlights the statistical significance of the findings ($p < 0.0001$ for DSS versus control; $p < 0.05$ for DSS versus TMZ), thereby further validating the impact of TMZ.

TMZ Attenuated Serum Level of IFN-γ and NF-kB-Associated DSS-Induced UC- BALB/c Mice

Dectin-1 stimulation prompts inflammatory signaling through the NF-kB pathway. Increased expression of LRRK2 has been observed to amplify Dectin-1-mediated cytokine responses by

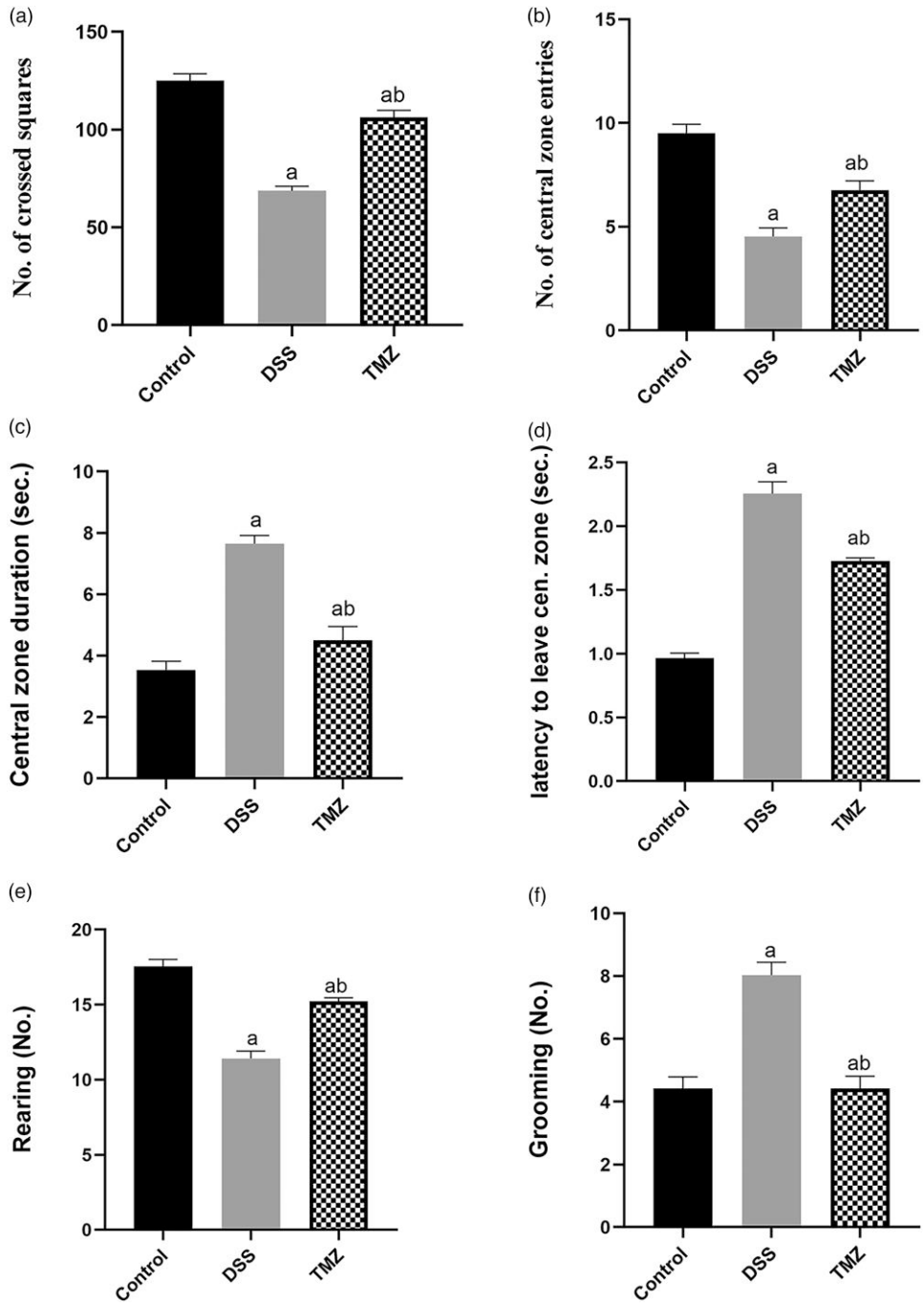

Fig. 2. The effect of TMZ (20 mg/kg/day/p.o.) for 4 weeks on OFT in the DSS model of UC. (**a**) Total number of crossed squares; (**b**) frequency entering the central zone; (**c**) central zone duration; (**d**) latency to leave the central zone; (**e**) frequency of rearing; and (**f**) frequency of grooming. Data are presented as mean ± SD, $n = 6$. a Significant difference from the control group, b Significant from DSS group (**a, b, d, e,** and **f**: $p < 0.0001$a; **c:** $p < 0.01^{a}$; **a**: $p < 0.05^{b}$; **b, c, d, e & f:** $p < 0.0001^{b}$), using one-way ANOVA test.

interacting with NF-kB signaling components. Toward this end, the present study concentrated on evaluating the expression of NF-kB 1 in serum and investigated its interaction with the Dectin-1 and LRRK2 signaling cascade and the role of TMZ in modulating this pathway. As shown in Fig. 5a, the administration of DSS displayed a significant increase ($p < 0.0001$) in the DSS group (254.3 ± 3.023) compared to the control group (120.0 ± 3.858), Furthermore, treatment with TMZ resulted in a marked reduction in serum NF-kB levels in the TMZ group (170.7 ± 1.675), contrasting with the elevated levels observed in the DSS group. These findings suggested that the potential function of TMZ may be linked to its capacity to regulate pathways of inflammation associated with NF-κB dysregulation. IFN-γ, a critical immune response driver, has been shown to upregulate LRRK2 expression, and subsequent overexpression increases inflammation in PD and UC. The interaction between IFN-γ and LRRK2 is critical in the pathogenesis of both disorders. Our findings revealed a significant ($p < 0.0001$) increase in serum levels of IFN-γ (123.9 ± 4.398) in the DSS-administered group when compared to the control group (38.84 ± 2.390). On the other hand, treatment with TMZ resulted in a marked

reduction in IFN-γ levels in comparison to the DSS group (62.19 ± 4.710; Fig. 5b). These findings suggest that the potential effects of TMZ may stem from its capacity to regulate inflammatory pathways targeting IFN-γ. This effect may involve the Dectin-1/LRRK2 signaling cascade, which amplifies cytokine responses through NF-kB. Furthermore, the downregulation of IFN-γ underscores TMZ's broader anti-inflammatory potential in UC and other immune-related conditions.

TMZ Mitigates Fecal Calprotectin and FOB Levels in DSS-Induced UC in BALB/c Mice

Fecal calprotectin is a reliable indicator of gastrointestinal tract inflammation. Its applications include diagnosis, disease activity monitoring, and prediction of disease relapses. FOB, an immunochemical fecal biomarker, is imperative for evaluating mucosal healing. As shown in Fig. 6a, the administration of DSS resulted in a significant upregulation ($p < 0.0001$) in fecal calprotectin levels (113.9 ± 4.398) in the DSS group, as compared to the control group (10.75 ± 2.315), confirming inflammation. Concurrently, treatment with TMZ resulted in a marked reduction in fecal calprotectin levels in the TMZ group, in contrast to the DSS group (52.21 ± 4.716). The observation that fecal calprotectin levels decreased in the TMZ group suggests its therapeutic potential in mitigating inflammation. Moreover, the FOB levels in the DSS model of UC (Fig. 6b) exhibited a notable increase ($p < 0.0001$) in FOB levels (4.750 ± 0.7071) in the DSS group when compared to the control group (0.250 ± 0.4629). In contrast, the TMZ administration diminishes FOB levels to (1 ± 0.9258) in comparison to the DSS group. This finding indicates that TMZ has an alleviating effect on colonic damage induced by DSS.

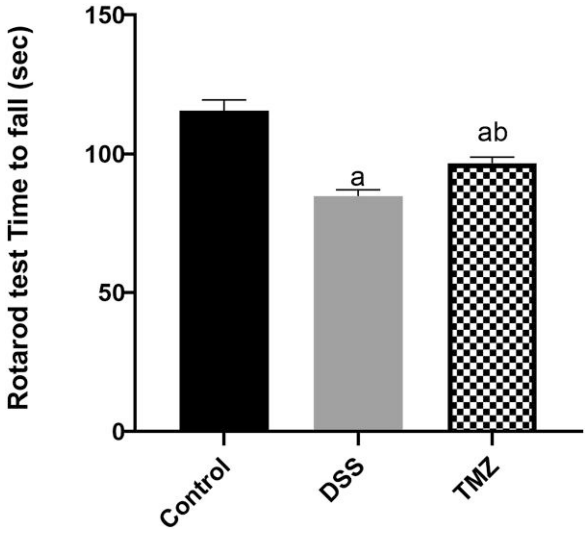

Fig. 3. The effect of TMZ (20 mg/kg/day/p.o) for 4 weeks on the rotarod test in the DSS model of UC. Data are presented as mean ± SD, $n = 6$. [a]Significant difference from the control group ($p < 0.0001$). [b] Significant from the DSS group ($p < 0.0001$ [b]), using a one-way ANOVA test.

TMZ Downregulated the Expression Brain and Colon Dectin-1, LRRK2 and αSyn in DSS-Induced UC-BALB/c Mice

In the current study, we investigated the impact of TMZ and the role of the Dectin-1/LRRK/αSyn-linked autophagy pathway in connecting UC to PD. The DSS group showed a significant increase in cerebral Dectin-1 expression (4.888 ± 0.3758 versus control 1.019 ± 0.05693, $p < 0.0001$) and colonic Dectin-1 (3.375 ± 0.2375 versus control 1.034 ± 0.02615, $p < 0.0001$), suggesting its involvement in UC-associated inflammation. TMZ administration downregulated both cerebral (2.138 ± 0.2973) and colonic (1.934 ± 0.1236) Dectin-1 expression when compared to the DSS group, indicating anti-inflammatory effects. For *LRRK2*, DSS induced marked upregulation in cerebral (6.388 ± 0.3682 versus control 1.025 ± 0.05976, $p < 0.0001$) and colonic tissues (5.330 ± 0.2753 versus control 1.025 ± 0.02204, $p < 0.0001$), supporting its involvement in colonic inflammation and neuroinflammation. TMZ was found to reduce expression in cerebral (3.050 ± 0.03024) and colonic tissues (2.284 ± 0.2129), suggesting restoration of cellular homeostasis. Subsequently, an

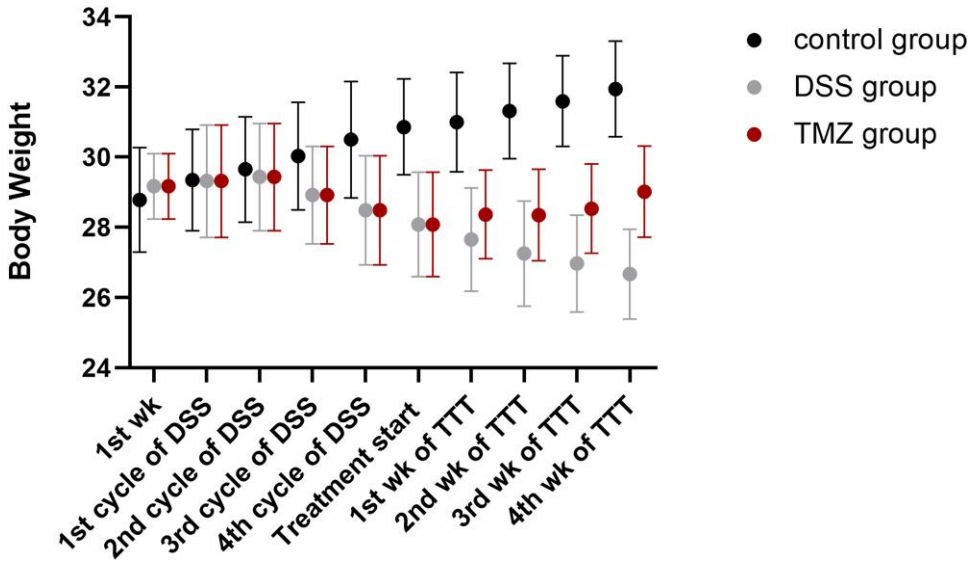

Fig. 4. The effect of TMZ (20 mg/kg/day/p.o) for 4 weeks on the body weight of mice in the DSS model of UC. Data are presented as mean ± SD, $n = 6$. [a]Significant difference from the control group ($p < 0.0001$ [a]), [b]Significant from the DSS group ($p < 0.05$[b]) using the repeated measure ANOVA test.

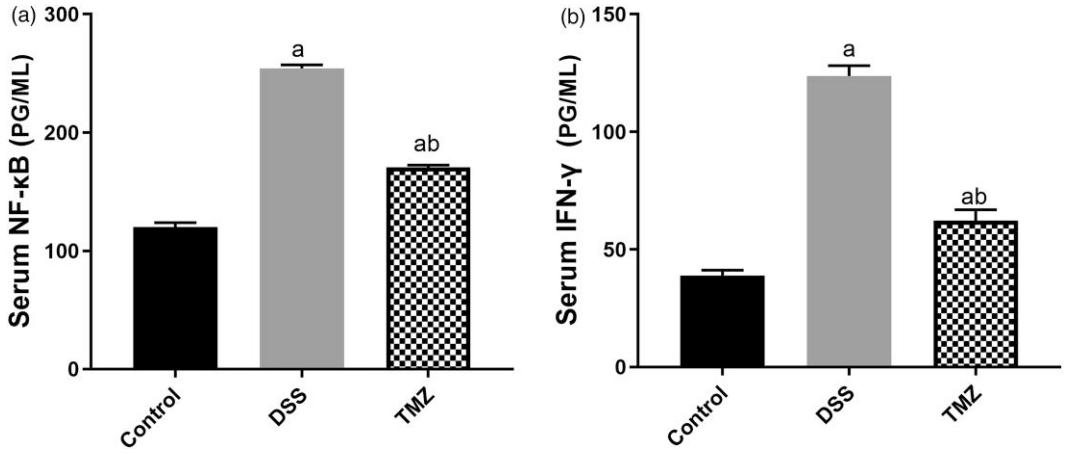

Fig. 5. The effect of TMZ (20 mg/kg/day/p.o) for 4 weeks on serum level of NF-κB (**a**) and IFN-γ (**b**) in DSS model of UC. Data are presented as mean ± SD, $n = 6$. [a] Significant difference from the control group ($p < 0.0001$[a]); [b] Significant difference from the DSS group ($p < 0.0001$[b]), using one-way ANOVA test followed by Tukey's multiple comparisons test.

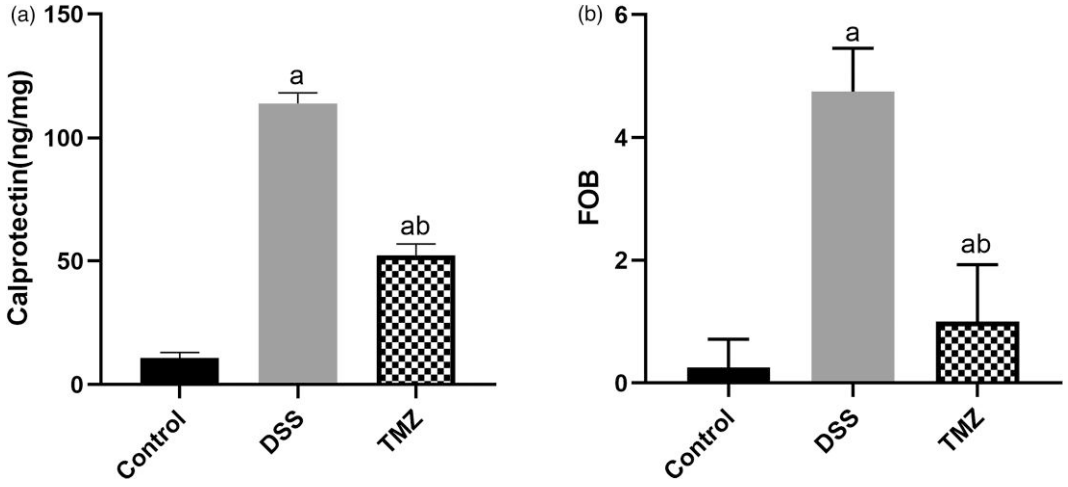

Fig. 6. (**a**) The effect of TMZ (20 mg/kg/day/p.o) for 4 weeks on Fecal calprotectin in DSS model of UC. Data are presented as mean ± SD, $n = 6$. a Significant difference from the control group ($p < 0.0001$[a]), [b]Significant difference from the DSS group ($p < 0.0001$[b]), using one-way ANOVA test followed by Tukey's multiple comparisons test. (**b**) The effect of TMZ (20 mg/kg/day/p.o) for 4 weeks on FOB in stool in the DSS model of UC. Data are presented as mean ± SD, $n = 6$. [a]Significant difference from the control group ($p < 0.0001$[a]), [b]Significant difference from the DSS group ($p < 0.0001$[b]), using one-way ANOVA test followed by Tukey's multiple comparisons test.

investigation was conducted into αSyn, a presynaptic protein involved in the regulation of neurotransmitter release, to explore the mechanism by which αSyn links UC and PD. Our results showed that the DSS-administered group revealed a significant upregulation in cerebral α-synuclein (4.213 ± 0.3441 versus control 1.043 ± 0.0337, $p < 0.0001$) and colonic α-syn (3.388 ± 0.2475 versus control 1.040 ± 0.03295, $p < 0.0001$). The TMZ-administered group displayed a significant downregulation of cerebral (1.728 ± 0.2349) and colonic (1.350 ± 0.1773) α-syn levels, potentially attenuating inflammation (Fig. 7). These findings demonstrate that TMZ alleviates UC and PD progression by targeting Dectin-1, *LRRK2*, and α-syn signaling pathways. The GTEx human expression data for *SNCA*(α-syn), *LRRK2*, and *CLEC7A* (Dectin-1) provide valuable physiological reference points that complement our murine model. Considering cross-species comparisons, the conserved roles of these PD-associated markers in humans and mice serve to strengthen the translational relevance of our findings. Notably, *SNCA* (α-synuclein) demonstrates expression in colonic tissues (sigmoid colon: 7.028 TPM; transverse colon: 2.094) with elevated levels in the substantia nigra (20.81 TPM), highlighting its role in gastrointestinal and neurological processes. *LRRK2* demonstrates expression in the sigmoid colon (6.254 TPM), the transverse colon (2.579 TPM), and the substantia nigra (2.658 TPM), underscoring its systemic roles in vesicle trafficking and cellular homeostasis. *CLEC7A* (Dectin-1) maintains expression in both colonic (sigmoid colon: 5.711 TPM; transverse colon: 5.504 TPM) and cerebral (substantia nigra: 3.855 TPM) tissues, emphasizing its importance in immune modulation and tissue-specific functions. These baseline profiles (Fig. 8), presented as box plots showing median with 25th and 75th percentiles (outliers marked beyond 1.5×IQR), provide essential references for interpreting gene dysregulation in our DSS-induced model and TMZ's regulatory effects.

TMZ-Enhanced Western Blot Analysis of Autophagy Markers P62 and LAMP2 Expression in DSS-induced UC-BALB/c Mice

The present study aims to investigate the effect of TMZ on the levels of the autophagy markers P62 and LAMP2 in the brains

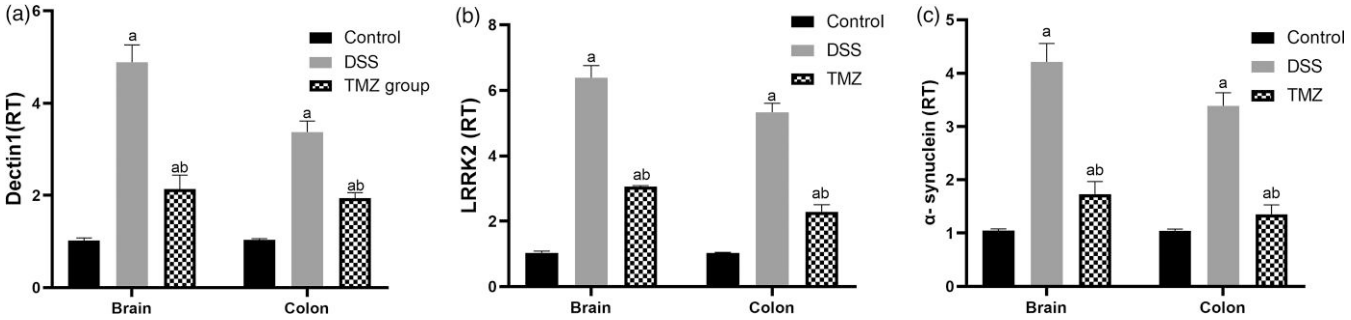

Fig. 7. The effect of TMZ (20 mg/kg/day/p.o) for 4 weeks on mice brain and colon Dectin-1in DSS model of UC (**a**). Data are presented as mean ± SD, $n = 6$. [a]significant difference from the control group ($p < 0.0001$a), [b] Significant difference from the DSS group ($p < 0.0001^{b}$), using one-way ANOVA test followed by Tukey's multiple comparisons test. (**b**) The effect of TMZ (20 mg/kg/day/p.o) for 4 weeks on the mouse brain and colon LRRK2 in DSS model of UC. Data are presented as mean ± SD, $n = 6$. a significant difference from control group ($p < 0.0001$a), b Significant difference from the DSS group ($p < 0.0001$b), using one-way ANOVA test followed by Tukey's multiple comparisons test (**c**). The effect of TMZ (20 mg/kg/day/p.o) for 4 weeks on mice brain and colon αSyn in DSS model of UC. Data are presented as mean ± SD, $n = 6$. [a] significant difference from control group ($p < 0.0001^{a}$), [b] Significant difference from DSS group ($p < 0.0001^{b}$), using one-way ANOVA test followed by Tukey's multiple comparisons test(C).

of BALB/c mice with DSS-induced UC. Autophagy dysregulation plays a key role in the pathogenesis of UC. P62 (SQSTM1), a selective autophagy receptor, facilitates the recruitment of cellular waste to autophagosomes for degradation, while LAMP2 is essential for lysosomal fusion and autophagy degradation. Impairment of either marker disrupts autophagy. Disruptions in autophagy have been associated with cellular stress, inflammation, and the exacerbation of UC pathology. P62, a selective autophagy receptor, accumulates during autophagy impairment. In DSS-treated mice, P62 levels exhibited a significant increase (5.638 ± 0.3335 versus control 1.026 ± 0.02264, $p < 0.0001$), suggesting an occurrence of autophagy dysfunction. The administration of TMZ led to a reduction in P62 accumulation (2.810 ± 0.2253), suggesting partial restoration of autophagy. Concurrently, the level of LAMP2, a critical component of lysosomal degradation, exhibited a marked decrease in DSS mice (6.825 ± 0.2915 versus control 1.038 ± 0.02915). The TMZ-revered pattern LAMP2 (3.821 ± 0.2061), implying improved lysosomal function. Quantitative Western blot analysis confirmed significant alterations in P62 and LAMP2 expression patterns. DSS-treated mice exhibited characteristically dense P62 bands and faint LAMP2 bands, an indication of impaired autophagic flux. TMZ administration reversed these effects, reducing P62 accumulation while enhancing LAMP2 expression. These coordinated changes demonstrate TMZ's capacity to restore the autophagic function in DSS-induced colitis, potentially through modulation of both autophagosome formation and lysosomal degradation pathways (Fig. 9). These reciprocal changes demonstrate TMZ's ability to restore autophagy flux in DSS-induced UC.

However, whether this occurs through direct (e.g., Adenosine monophosphate protein Kinase [AMPK]/ Mammalian Target Of Rapamycin [mTOR]) or secondary to anti-inflammatory mechanisms requires further investigation, including LC3-II flux and autophagosome–lysosome fusion assays. The GTEx human expression data for LAMP2 and SQSTM1 (P62) provide valuable physiological reference points that complement our murine model. Considering cross-species comparisons, the conserved roles of these autophagy markers in humans and mice strengthen the translational relevance of our findings. Notably, LAMP2 expression levels in colonic tissues (transverse colon: 20.45 TPM; sigmoid colon: 24.41 TPM) exhibited elevated levels in the substantia nigra (46.29 TPM). In contrast, P62 shows particularly high levels of expression in colonic tissue (81.21 TPM) in comparison to substantia nigra (30.14 TPM), a region implicated in Parkinson's disease. These baseline profiles provide a valuable framework for interpreting the changes in LAMP2 and P62 expression observed in the DSS-induced ulcerative colitis model and the modulatory effects of TMZ treatment (Fig. 10).

Histopathological Studies

Colon H&E

TMZ Administration Profile on Colon Diameter, Mucosal, and Thickness Levels in DSS-Induced UC in BALB/c Mice

This study evaluates the histopathological changes in colonic structure among control, DSS-induced UC, and TMZ-treated DSS groups in DSS-induced UC- BALB/c mice. The colon of the control group appears normal in length and has no signs of bleeding to the naked eye. Light microscopic examination of H&E-stained transverse sections of the mice colon in the control group showed the wall of the colon. The lumen is lined by folded mucosa and surrounded by smooth muscles (Muscularis externa) and a layer of flat epithelial cells (Serosa). The mucosa comprises a layer of epithelial cells, lamina propria, and muscularis mucosa. The epithelial surface forms deep invaginations called intestinal glands or crypts. The intestinal lumen and the crypts are lined by columnar absorptive cells, with oval basal nuclei and apical microvilli (brush border), and a large number of goblet cells, with foamy cytoplasm and basal flattened nuclei (Figs. 11a–11c). The colonic diameter of this group (in μm) was (1282 ± 8.911), and the mucosal thickness (in μm) was (548.8 ± 2.435; Fig. 12).

The DSS group showed shrunken, distorted mucosal folds and a decrease in colon length with signs of bleeding in the naked eye appearance (Fig. 11d). The mucosa showed focal areas of lost epithelial lining. The epithelial lining cells were desquamated in the lumen (Fig. 11e). Goblet cells were seen to be destroyed. Significant mononuclear cellular infiltration was observed in the lamina propria and the mucosa between the intestinal glands, spanning the whole thickness of the mucosa. Dilated blood vessels are seen in the submucosa. Extravasated red blood cells were present in the mucosa (Figs. 11f and 11g). The colonic diameter (in μm) was (476.8 ± 2.435), and the mucosal thickness (in μm) was

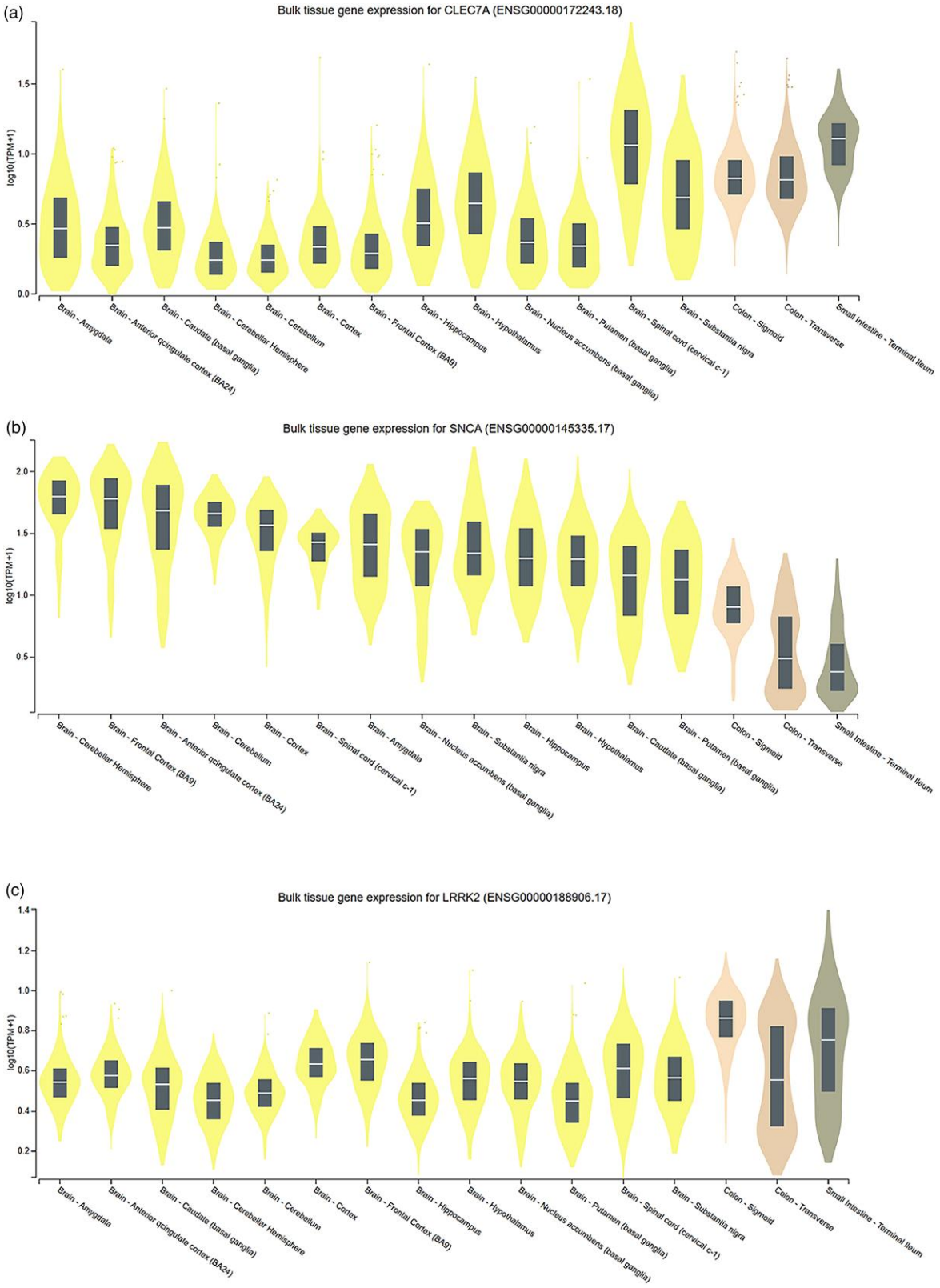

Fig. 8. Gene expression profiles of SNCA (α-synuclein, ENSG00000145335.15), LRRK2 (ENSG00000188906.14), and CLEC7A (Dectin-1, ENSG00000172243.17) in normal colon and brain tissues, measured in transcripts per million (TPM) from the GTEx Portal. Data represent baseline expression levels: SNCA (sigmoid colon: 7.028 TPM; transverse colon: 2.094 TPM; substantia nigra: 20.81 TPM); LRRK2 (sigmoid colon: 6.254 TPM; transverse colon: 2.579 TPM; substantia nigra: 2.658 TPM); CLEC7A (sigmoid colon: 5.711 TPM; transverse colon: 5.504 TPM; substantia nigra: 3.855 TPM). Box plots show median with 25th–5th percentiles (outliers: >1.5×IQR).

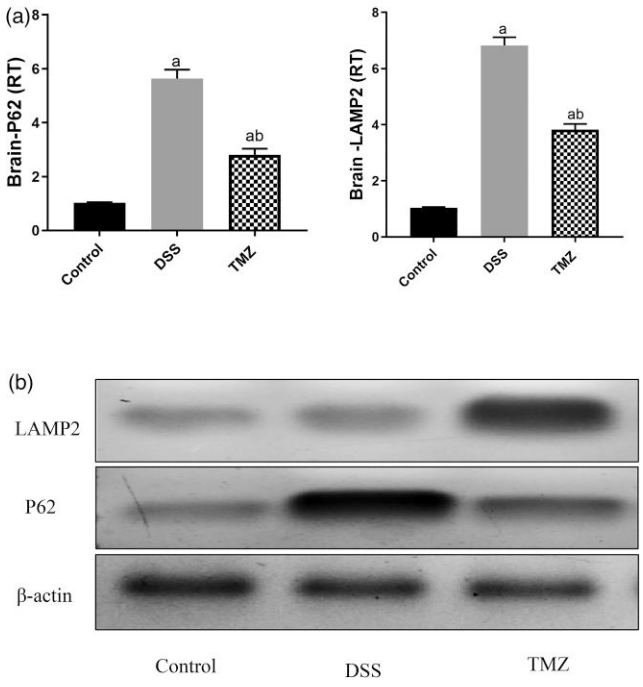

Fig. 9. Effects of TMZ treatment (20 mg/kg/day p.o., 4 weeks) on autophagy markers P62 and LAMP2 in brain tissue of DSS-induced ulcerative colitis mice. (**a**) Quantitative analysis showing protein expression levels (mean ± SD, $n = 6$) with a indicates significant difference from the control group ($p < 0.0001$) and b indicates significant difference from the DSS group ($p < 0.0001$) by one-way ANOVA with Tukey's post-hoc test. (**b**) Representative Western blot images demonstrating P62 (~62 kDa), LAMP2 (~110 kDa), and β-actin (~42 kDa, loading control) protein expression across experimental groups (Control, DSS, TMZ) with molecular weight markers indicated.

(297.3 ± 1.832); both measurements were significantly decreased as compared to the control group (Fig. 12).

The TMZ group showed an average diameter of the colon and average thickness of the wall with less decrease in colon length and fewer signs of bleeding (Fig. 11h). The mucosa was intact. The absorptive epithelial cells were intact, with oval basal nuclei and preserved brush border (BB). Goblet cells were seen with foamy cytoplasm and basal flattened nuclei. Some mononuclear inflammatory cells were observed in the lamina propria and submucosa. No dilated blood vessels were seen in the submucosa. No extravasated red blood cells were detected (Figs. 11i and 11j). The colonic diameter (in μm) was (878.9 ± 2.232), and the mucosal thickness (in μm) was (450.1 ± 3.137); both parameters were significantly increased as compared to the DSS group (Fig. 12).

Colon Mallory's Trichrome

TMZ Administration Profile on Area% of Collagen Fibers in the Submucosa and Lamina Propria of the Colon in DSS-Induced UC in BALB/c Mice

Light microscopic examination of Mallory's trichrome-stained transverse sections of the colon of mice in the control group showed the distribution of blue-stained collagen fibers (↑) in the colon's wall. A few long, wavy collagen bundles were present in the submucosa and between the intestinal glands (Figs. 13a and 13b). The area % of collagen fibers was (8.344 ± 1.517). The DSS group had an elevated quantity of collagen fibers in the colonic wall. The submucosa exhibited an augmented presence of dense, undulating collagen bundles. Numerous slender collagen fibers were observed in the lamina propria spreading toward the digestive glands (Fig. 13c and 13d). The area % of collagen fibers was (18.47 ± 1.056), which was increased compared to the control group. The TMZ group showed an average amount of collagen fibers in the colon's wall, a few long, wavy collagen bundles in the submucosa (Fig. 13e and 13f). The area % of collagen fibers was (12.58 ± 1.036), which decreased compared to the DSS group (Fig. 14).

Brain H&E

Light microscopic examination of H&E-stained sections of the midbrain of mice in the control group showed the substantia nigra as a group of nerve cells in the anterior part of the crus cerebri. The medial part of the substantia nigra is formed of the pars compacta, while its lateral part forms the pars reticularis. Nerve cells (neurons) in the substantia nigra are large, multipolar neurons; each neuron has basophilic cytoplasm and a large, rounded, central, vesicular nucleus with a prominent nucleolus. Glial cells' nuclei are seen as small, dark nuclei between the nerve cells. The neuropil appears homogenous (Figs. 15a and 15b). Light microscopic analysis of H&E-stained slices of the midbrain in mice from the DSS group revealed many deeply stained cells. Most of the nerve cells are shrunken and surrounded by a clear hollow. They have dark cytoplasm and small, deeply stained nuclei. Small nuclei of

Different types of glial cells are seen. The neuropil shows many vacuoles (Figs. 15c and 15d). Light microscopic examination of H&E-stained sections of the midbrain of mice in the TMZ group showed the substantia nigra with regular distribution of neurons. Most neurons have large central vesicular nuclei with prominent nucleoli and granular basophilic cytoplasm. Small nuclei of different types of glial cells are also seen. The neuropil appears homogenous (Figs. 15e and 15f).

Immunohistochemistry Analysis

TMZ Administration Profile on the Number of Immunoreactive Cells to TH in DSS-Induced UC in BALB/c Mice

Examination of midbrain sections immunohistochemically stained with anti-TH in the control group showed the distribution of dopaminergic neurons in the substantia nigra. Positive immune reaction to anti-TH appeared as dark brown granules in the cytoplasm of some neurons (dopaminergic neurons), especially in the pars compacta of the substantia nigra (Figs. 16a and 16b). The number of neurons with positive immune reaction to anti-TH was (12.88 ± 1.642) (Fig. 17). Examination of midbrain sections immunohistochemically stained with anti-TH in the DSS group showed a negative immune reaction to TH in the cytoplasm of most neurons in the substantia nigra. Few neurons showed a weak immune reaction to TH (Fig. 16c). The mean ± SD number of neurons with positive immune reaction to anti-TH was (3.375 ± 1.408) (Fig. 17). Examination of midbrain sections immunohistochemically stained with anti-TH in the TMZ group showed positive immune reaction to tyrosine hydroxylase in many neurons in the substantia nigra (Fig. 16d). The number of neurons with positive immune reaction to anti-TH was (8.125 ± 0.834) (Fig. 17).

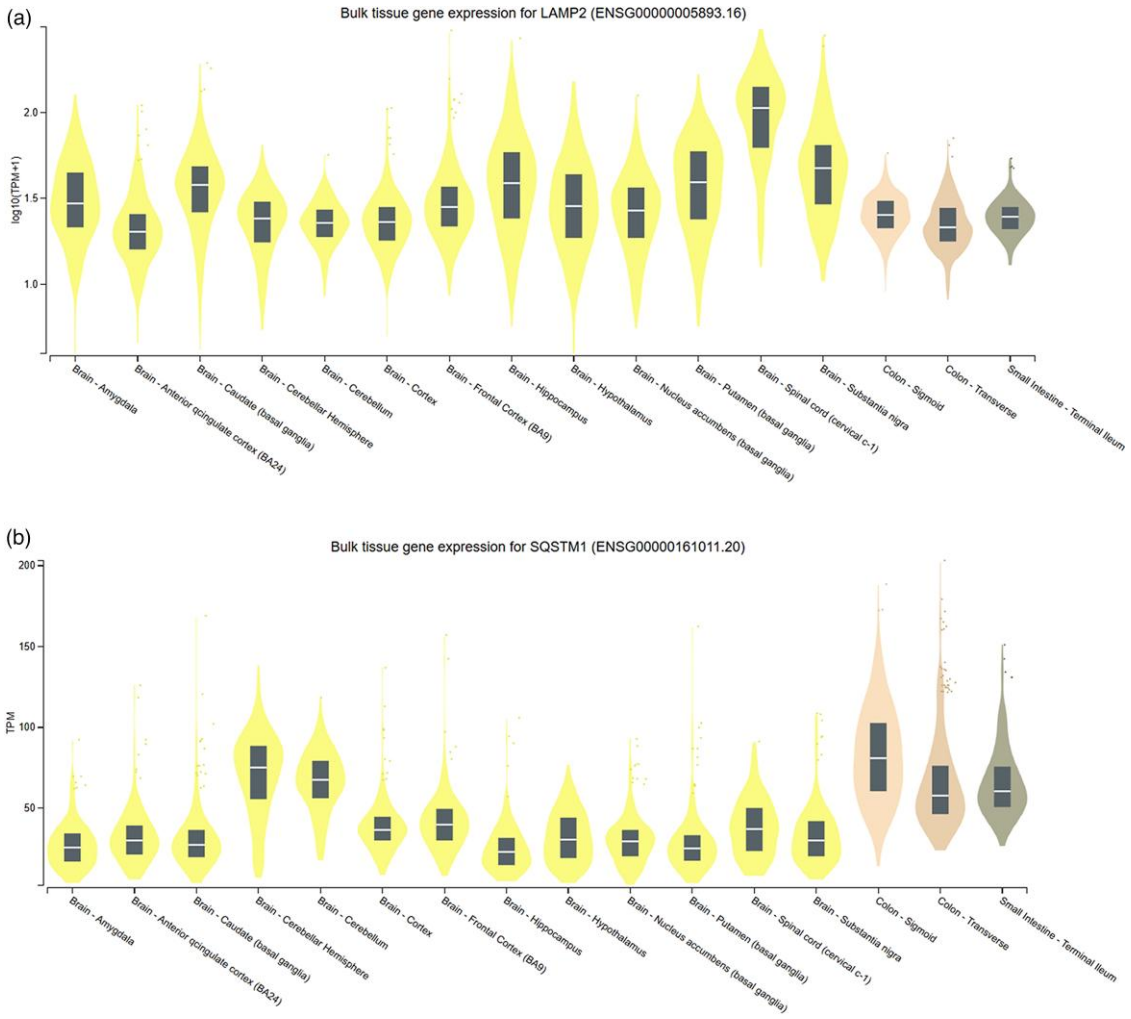

Fig. 10. (**a**) Baseline gene expression data from the GTEx Portal (measured in TPM) for autophagy markers: LAMP2 (transverse colon: 20.45 TPM; sigmoid colon: 24.41 TPM; substantia nigra: 46.29 TPM) and (**b**) SQSTM1/P62 (transverse colon: 81.21 TPM; substantia nigra: 30.14 TPM) in normal tissues.

TMZ Administration Profile on the Number of Immunoreactive Cells to αSyn in DSS-Induced UC in BALB/c Mice

Examination of midbrain sections immunohistochemically stained with anti-*α*Syn in the control group showed almost all neurons with a negative immune reaction to anti-*α*Syn. Few cells showed minimal reaction (Fig. 18a). The number of neurons with a positive immune reaction to anti-*α*Syn was (2.375 ± 1.508) (Fig. 19). Examination of midbrain sections immunohistochemically stained with anti-TH in the DSS group showed a markedly increased number of neurons with a positive immune reaction to anti-*α*Syn in the substantia nigra as compared to the control group. The positive immune reaction appeared as a dark brown reaction in the cytoplasm and processes of the neurons (Fig. 18b). The number of neurons with a positive immune reaction to anti-*α*Syn was (18.13 ± 1.458) (Fig. 19). Examination of midbrain sections immunohistochemically stained with anti-*α*Syn in the TMZ group showed a markedly decreased number of neurons with positive immune reaction to anti-*α*Syn in the substantia nigra as compared to the model group (Fig. 18c). The number of neurons with positive immune reaction to anti-*α*Syn was (7.625 ± 1.061) (Fig. 19).

Molecular Docking Study

TMZ displayed modest, target-dependent predicted binding free energies (ΔG) across the three proteins (Supplementary Table S1). The most favorable TMZ score was observed for LRRK2 (-6.36 kcal·mol^{-1}), followed by Dectin- (-5.76 kcal·mol^{-1}) and the *α*-synuclein fibril (-5.55 kcal·mol^{-1}). As intended, each positive control ligand anchored its corresponding system: Laminarin for Dectin-1, LRRK2-IN-1 for LRRK2, and EGCG for α-synuclein. LRRK2-IN-1 exhibited the most favorable overall docking score (-9.39 kcal·mol^{-1}). It reproduced the crystallographic pose with a very low heavy-atom RMSD (0.115 Å), supporting correct grid placement and parameterization for that receptor. Differences between TMZ and the control ligands in Dectin-1 and *α*-synuclein were small ($\leq$0.21 and 0.54 kcal·mol^{-1}, respectively) and lie within the expected error margin of a single AutoDock4 scoring function.

TMZ docked into the carbohydrate-recognition domain, forming a hydrogen-bond network involving Lys128, Asp158, and Asn159. An additional π–anion interaction was predicted between the electron-deficient region of TMZ's heterocycle and the side-chain carboxylate of Asp158, with a supplementary

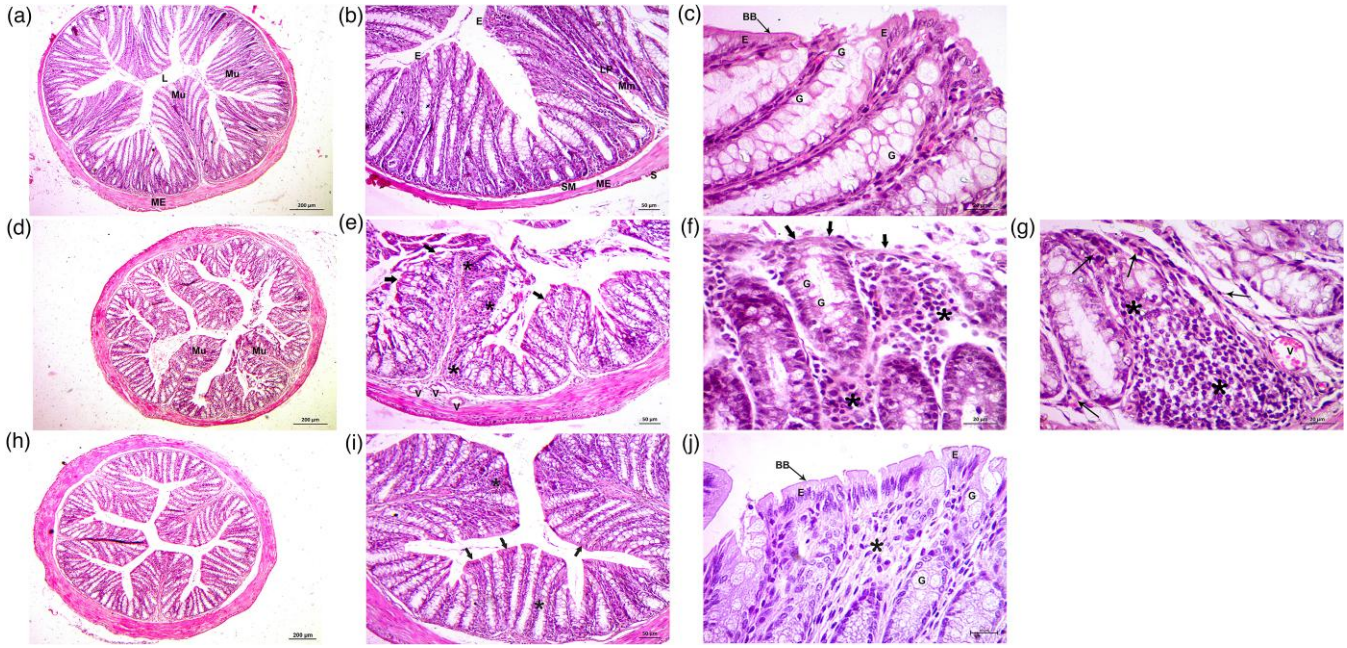

Fig. 11. A photomicrograph of a transverse section in the mice colon (**a-c**)**:** *control* group showing the wall of the colon. (**a**) The lumen (L) is lined by folded mucosa (Mu) and surrounded by the muscularis externa (ME), H&E × 40. (**b**) The mucosa of the colon formed of a layer of epithelial cells (E), lamina propria (LP), and muscularis mucosa (Mm). The mucosa is surrounded by the submucosa (SM), the muscularis externa (ME), and the serosa (S), H&E × 100. (**c**) The intestinal glands lined by columnar absorptive epithelial cells (E) having oval basal nuclei and apical thin brush border (BB), and numerous goblet cells (G) with foamy cytoplasm and basal flattened nuclei, H&E × 400. (**d-g**): *DSS* group (**d**) showing shrunken, distorted mucosal folds (Mu), H&E × 40. (**e**) The mucosa shows focal areas of lost epithelial lining (thick arrows). Extensive mononuclear cellular infiltration is seen in the mucosa (*). Dilated blood vessels are seen in the submucosa (V), H&E × 100. (**f**) An area in the mucosa with desquamated epithelial lining cells (Thick arrows). Goblet cells are seen as destroyed (G). Extensive mononuclear cellular infiltration is seen in the mucosa (*) between the intestinal glands, H&E × 400. (**g**) A large area of mononuclear cellular infiltration (*) spanning the whole thickness of the mucosa. A dilated, congested blood vessel (V) is seen. Extravasated red blood cells are present (↑), H&E × 400. (**h-j**): *treated* (TMZ) group (**h**) shows average colon diameter and average wall thickness, H&E × 40. (**i**) Intact mucosa (Thick arrows). Some mononuclear inflammatory cells are seen in the lamina propria (*). No dilated blood vessels are seen in the submucosa, H&E × 100. (**j**) Intact absorptive epithelial cells (E) with oval basal nuclei and preserved brush border (BB). Goblet cells (G) are intact, with foamy cytoplasm and basal flattened nuclei. Some mononuclear cells are in the lamina propria (*), H&E × 400.

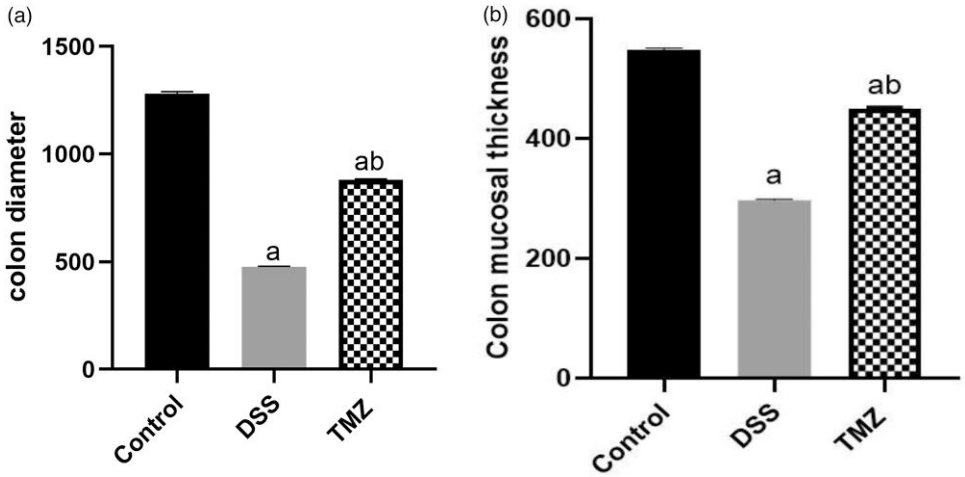

Fig. 12. (**a**) The effect of TMZ (20 mg/kg/day/p.o) for 4 weeks on colon diameter in DSS model of UC: Data are presented as mean ± SD, $n = 6$. A significant difference from control group ($p < 0.0001$a), b Significant difference from DSS group ($p < 0.0001$b), using one-way ANOVA test followed by Tukey's multiple comparisons test. (**b**) The Effect of TMZ (20 mg/kg/day/p.o) for 4 weeks on colon mucosal thickness in DSS model of UC: Data are presented as mean ± SD, $n = 6$. a Significant difference from control group ($p < 0.0001$a), b Significant difference from DSS group ($p < 0.0001$b), using one-way ANOVA test followed by Tukey's multiple comparisons test.

hydrogen bond to Asn159 stabilizing the orientation (Fig. 20a). Laminarin—used here as a β-1,3-glucan reference—formed hydrogen bonds with Asp158 and Asn159, recapitulating canonical carbohydrate-recognition features of C-type lectin carbohydrate-binding grooves (Fig. 20b). The overlap in key polar contacts (Asp158 and Asn159) between TMZ and Laminarin and the small difference in predicted ΔG (TMZ −5.76 versus Laminarin −5.73 kcal·mol^{-1}) suggest the docking

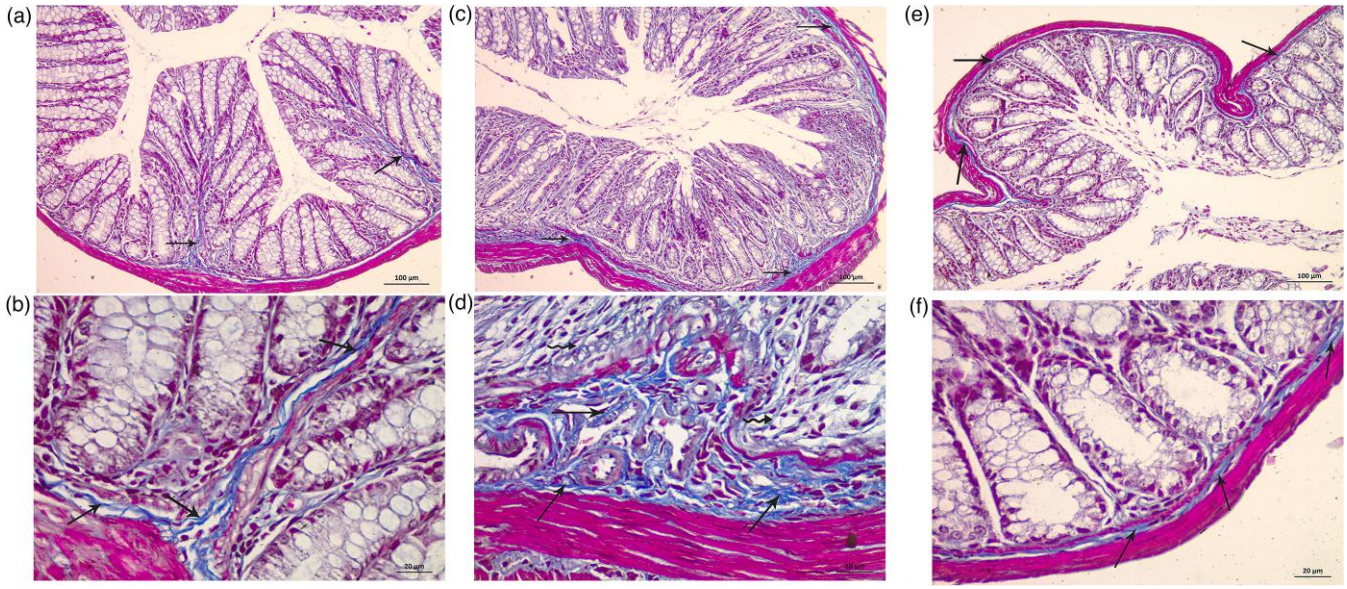

Fig. 13. A photomicrograph of a transverse section in the colon of a mice (**a&b**): *control* group, (**a**) showing the distribution of blue-stained collagen fibers (↑) in the wall of the colon, Mallory' trichrome stain × 40. (**b**) A few long, wavy collagen bundles (thin arrows) in the submucosa and between the intestinal glands, Mallory' trichrome stain × 400. (**c & d**): *model* group, (**c**) exhibiting an increased quantity of collagen fibers in the wall of the colon (↑), Mallory' trichrome stain × 40. (**d**) increased amount of thick, wavy collagen bundles in the submucosa (↑). Many thin collagen fibers are seen in the lamina propria (wavy arrows) extending to the intestinal glands, Mallory' trichrome stain × 400. (**e & f**)**:** *treated* group, (**e**) showing collagen fibers in the colon wall (↑). Mallory' trichrome stain × 40. (**f**) Few long, wavy collagen bundles in the submucosa (↑), Mallory' trichrome stain × 400.

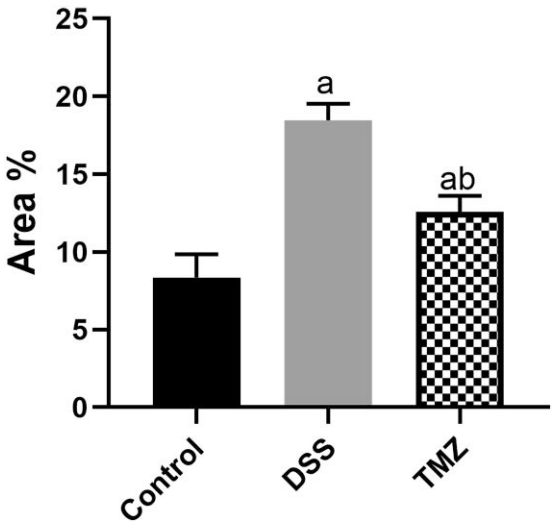

Fig. 14. The effect of TMZ (20 mg/kg/day/p.o.) for 4 weeks on area% of collagen fibers in submucosa and Lamina propria of colon in DSS model of UC: Data are presented as mean ± SD, $n = 6$. a Significant difference from the control group ($p < 0.0001$a), b Significant difference from DSS group ($p < 0.0001$b), using one-way ANOVA test followed by Tukey's multiple comparisons tests.

procedure correctly highlighted the principal polar anchor points of the cleft.

Within the kinase domain, TMZ engaged Lys1034 through hydrogen bonding and established multiple hydrophobic/π interactions (π–σ with Leu1161; π–alkyl with Ala1176 and Val1040), indicative of shallow hydrophobic accommodation in the ATP hinge vicinity (Fig. 20a). In contrast, the reference inhibitor LRRK2-IN-1 achieved a substantially more favorable predicted energy (−9.39 kcal·mol^{-1}) and an internally validated pose (RMSD 0.115 Å relative to the crystallographic conformation). Its interaction pattern included a denser hydrogen-bond network (Lys1055, Val1108 backbone, Ile1032, Gly1111) plus π–σ and π–alkyl contacts with Leu1161 and Ala1176—residues also contacted by TMZ—highlighting partial overlap in spatial occupation (Fig. 21b). The magnitude of the ΔG gap (~3.0 kcal·mol^{-1}) between LRRK2-IN-1 and TMZ is consistent with the higher potency typically reported for optimized kinase inhibitors versus small, relatively polar scaffolds like TMZ. This internal control thus substantiates that the docking setup can differentiate a known high-affinity ligand from a structurally distinct test compound.

For the α-synuclein fibril surface cavity, TMZ achieved a ΔG of −5.55 kcal·mol^{-1} via three principal hydrogen bonds involving Ala56 and Lys58, stabilizing the pose (Fig. 22a). EGCG, docked as a literature-supported fibril modulator, produced a slightly less favorable score (−5.01 kcal·mol^{-1}) but formed a richer polar interaction network: individual hydrogen bonds to Thr54 and Lys58, a triad of hydrogen bonds with Glu61 (reflecting EGCG's polyphenolic multi-donor/acceptor capacity), and an amide–π stacking interaction with Thr72 or the adjacent backbone. The broader contact surface of EGCG is qualitatively consistent with its reported ability to remodel or interfere with fibril aggregation interfaces (Fig. 22b).

Molecular Dynamics Simulations

All three TMZ–protein complexes—Dectin-1 (PDB ID: 2BPH), LRRK2 (PDB ID: 4YZM), and α-synuclein fibril (PDB ID: 6A6B)—underwent 100 ns production molecular dynamics (MD) simulations. Following equilibration, the systems exhibited no major instabilities, such as energy spikes, vacuum bubbles, or runaway coordinates, confirming that the initial docked complexes were suitable for extended timescale sampling.

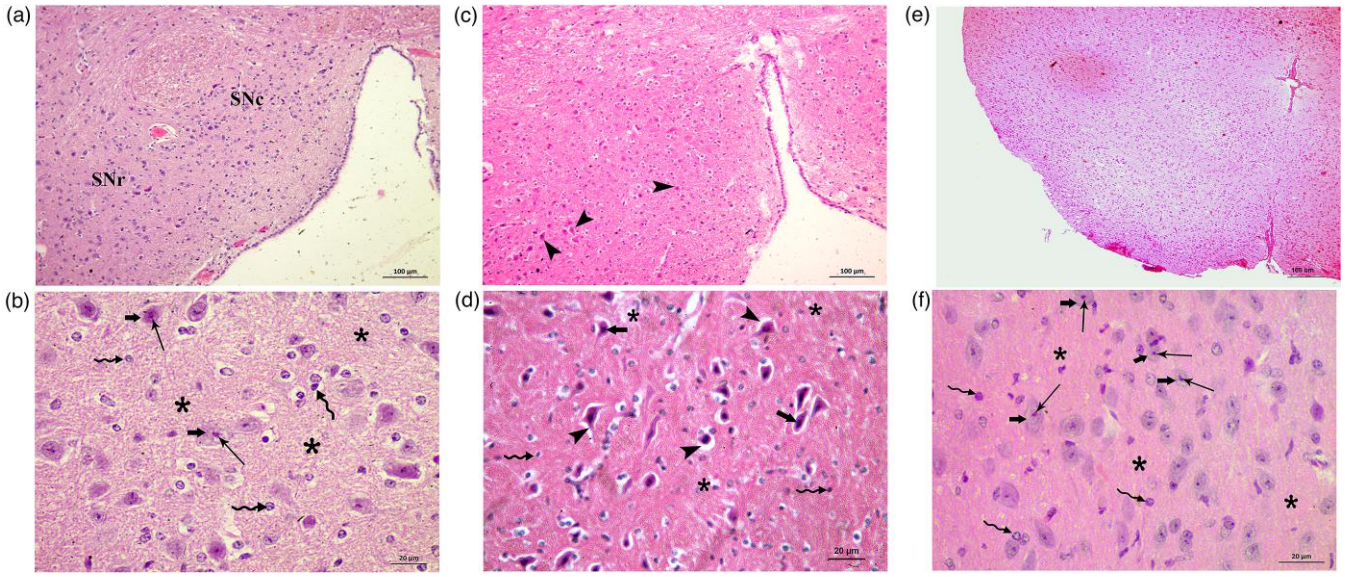

Fig. 15. A photomicrograph of a section in the midbrain of mice (**a & b**): control group, (**a**) showing the substantia nigra in the anterior part of the crus cerebri. The medial part of the substantia nigra forms the pars compacta (SNc), while the lateral part forms the pars reticularis (SNr), H&E × 100. (**b**) showing neurons in the substantia nigra. The neurons are large, with large central vesicular nuclei (thick arrows), prominent nucleoli (thin arrows), and granular basophilic cytoplasm. Small nuclei of different types of glial cells (wavy arrows) are also seen. The neuropil (*) appears homogenous, H&E × 400. (**c & d**): Model group, (**c**) showing the substantia nigra. Notice the presence of many deeply stained neurons (Arrowheads), H&E × 100. (**d**) Most neurons are shrunken and surrounded by a clear hollow (Arrowheads). They have dark cytoplasm and small, deeply stained nuclei (Thick arrows). Many nuclei of different glial cell types are shrunken and deeply stained (Wavy arrows). The neuropil shows many vacuoles (*), H&E × 400. (**e & f**): treated group, (**e**) showing the substantia nigra with regular distribution of neurons, H&E × 100. (**f**) showing neurons in the substantia nigra. Most of the neurons are large, having large central vesicular nuclei (thick arrows) with prominent nucleoli (thin arrows), and granular basophilic cytoplasm. Small nuclei of different types of glial cells (wavy arrows) are also seen. The neuropil appears homogenous (*), H&E × 400.

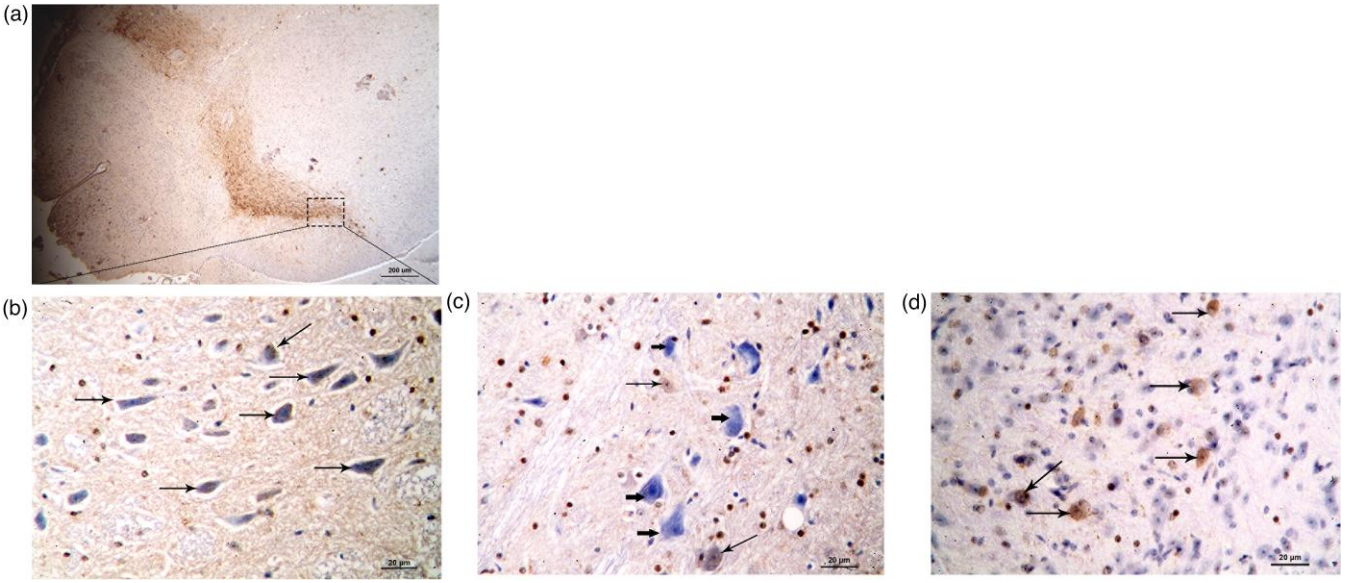

Fig. 16. A photomicrograph of a section in the midbrain of mice (**a & b**): control group, (**a**) showing the distribution of dopaminergic neurons in substantia nigra (rectangle and dotted lines denote magnified area in **b**), anti-TH × 100. (**b**) Neurons with a positive immune reaction to TH show brown granules in their cytoplasm (Thin arrows), Anti-TH × 400. (**c**) DSS group, showing a negative immune reaction to TH in the cytoplasm of most of the neurons (thick arrows) in the substantia nigra. Few neurons show a weak immune reaction to TH (thin arrows), Anti-TH × 400. (**d**) TMZ group, showing many neurons in the substantia nigra with a positive immune reaction to TH (thin arrows), Anti-TH × 400.

The RMSD profiles of TMZ (ligand heavy atoms) relative to the minimized starting structures demonstrated that the ligand adopted stable conformations across all three complexes (Fig. 23a). Among them, the LRRK2–TMZ complex displayed the highest stability, with RMSD fluctuations below 0.02 nm. The α-synuclein–TMZ complex exhibited moderate fluctuations between 0.05 and 0.12 nm, whereas the Dectin-1–TMZ complex showed slightly larger deviations ranging from 0.05 to 0.20 nm. In all cases, the RMSD curves reached a plateau and remained stable throughout the

simulation, suggesting that TMZ maintained its binding orientation in the active cavities.

Further confirmation of system stability was provided by the solvent-accessible surface area (SASA) analysis (Fig. 23b). The SASA values remained consistent, fluctuating minimally within 70–75 nm^2 for Dectin-1, 153–161 nm^2 for LRRK2, and 40–48 nm^2 for α-synuclein. These findings reinforce the conclusion that the protein structures retained compact conformations with stable solvent exposure profiles throughout the 100-ns trajectory.

To probe residue-level stability at the TMZ binding interfaces, backbone atom root mean square fluctuation (RMSF) profiles were computed over the 100-ns production trajectories (Figure S1A, S1C, S1E). In the Dectin-1–TMZ complex (Supplementary Fig. S1a), fluctuations across the fold were generally modest, and residues forming docking contacts—Gly127, Lys128, Asp158, and Asn159—showed suppressed mobility (<0.2 nm), indicating that the carbohydrate-recognition groove remained conformationally competent to sustain ligand engagement. This local rigidity supports the docking prediction that TMZ can hydrogen bond within the Laminarin-defined cavity. In the LRRK2–TMZ system (Supplementary Fig. S1c), the binding-site residues implicated by docking (Ile1032, Lys1034, Val1040, Leu1161, and Ala1176) also remained relatively immobile (<0.2 nm), consistent with a well-formed ATP/hinge pocket. The low RMSF at these positions helps explain the comparatively more favorable docking score for TMZ in LRRK2. By contrast, the α-synuclein fibril–TMZ simulation (Supplementary Fig. S1e) showed elevated global flexibility characteristic of solvent-exposed fibrillar surfaces; nevertheless, the local region surrounding the docking contacts (e.g., Ala56, and to a lesser extent Lys58) fluctuated less than adjacent segments, suggesting a shallow microenvironment capable of transient ligand retention. This localized motion damping agrees with the ligand RMSD stabilization observed in Figure 20a. To gain deeper insights into the binding stability, the number of hydrogen bonds formed between TMZ and the three proteins was monitored throughout the 100-nanosecond simulation.

Time-resolved hydrogen-bond counts between TMZ and each protein (Supplementary Figs. S1b, S1d, S1f) further contextualize the docking interaction patterns. In Dectin-1, one to two hydrogen bonds persisted through most of the 100-ns trajectory, with a third transient contact emerging intermittently toward the end of the simulation (Supplementary Fig. S1b). This dynamic 1–3 H-bond envelope aligns with the docking-predicted network involving Lys128, Asp158, and Asn159, though the MD data indicate that not all contacts are simultaneously maintained. In LRRK2, a more consistent two-hydrogen-bond pattern was sustained across the trajectory (Supplementary Fig. S1d), reinforcing the docking result that identified a strong polar anchor (Lys1034) within a relatively well-enclosed pocket augmented by hydrophobic residues (Val1040, Leu1161, and Ala1176). The stability of these interactions helps rationalize the more favorable ΔG predicted for TMZ in LRRK2 relative to the other targets. In the α-synuclein complex, two initial hydrogen bonds broke within ~5 ns, after which only a sporadic single contact was observed over the remainder of the simulation (Figure S1F). This rapid loss of persistent polar anchoring is consistent with the modest docking score and suggests that TMZ's retention at the α-synuclein surface is governed primarily by weak hydrophobic or nonspecific contacts, most notably in the Ala56 region identified in the docking stage.

End-point binding free energies (ΔG_bind, approximated as TOTAL) were estimated for TMZ in complex with Dectin-1

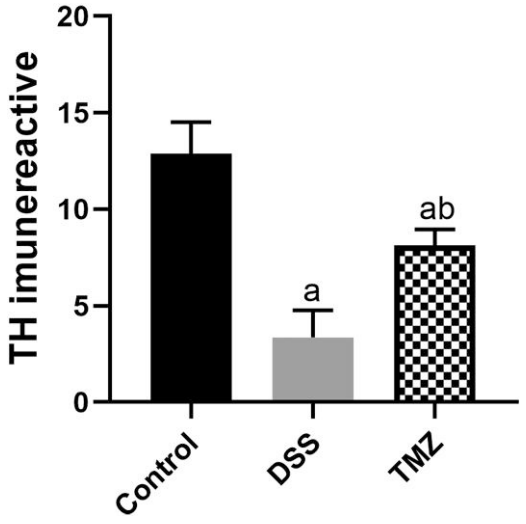

Fig. 17. The effect of TMZ (20 mg/kg/day/p.o) for 4 weeks on the number of immunoreactive cell to TH in the DSS model of UC: Data are presented as mean ± SD, $n = 6$. aSignificant difference from the control group ($p < 0.0001$a), bSignificant difference from DSS group ($p < 0.0001$b), using one-way ANOVA test followed by Tukey's multiple comparisons tests.

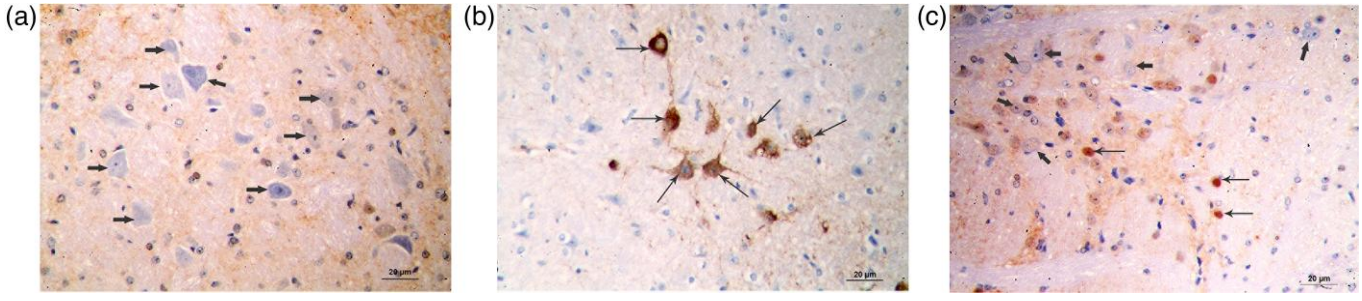

Fig. 18. A photomicrograph of a section in the midbrain of mice (**a**): control group showing nerve cells in the substantia nigra show negative anti αSyn immune reaction (thick arrows), anti αSyn × 400. (**b**): DSS group showing some nerve cells in the substantia nigra with a positive immune reaction to anti-αSyn seen as a dark brown stain in their cytoplasm and processes (thin arrows), anti-αSyn × 400. (**c**): TMZ group showing most of the nerve cells in the substantia nigra show negative anti-αSyn immune reaction (thick arrows). Notice the presence of a few nerve cells with positive reaction to anti-αSyn (thin arrows), anti-αSyn × 400.

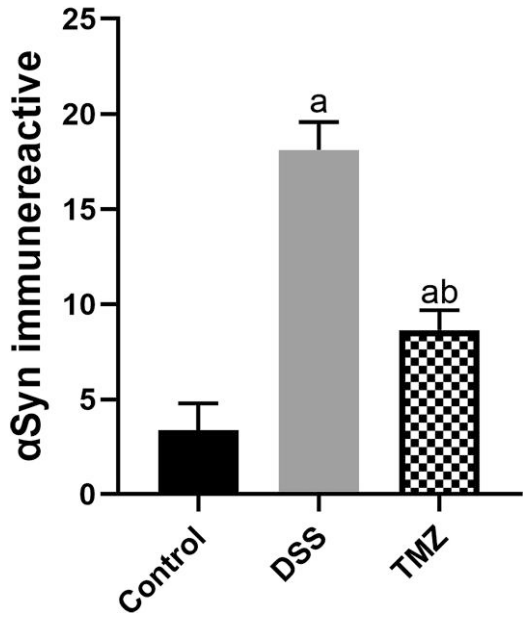

Fig. 19. The effect of TMZ (20 mg/kg/day/p.o) for 4 weeks on the number of immunoreactive cells to αSyn in DSS model of UC: Data are presented as mean ± SD, $n = 6$. aSignificant difference from control group ($p < 0.0001$a), bSignificant difference from DSS group ($p < 0.0001$b), using one-way ANOVA test followed by Tukey's multiple comparisons test.

(2BPH), LRRK2 (4YZM), and α-synuclein fibril (6A6B) using the MM-PBSA approach applied to production MD trajectories (Supplementary Figs. S2a–S2c; Table 2). All three systems yielded negative average TOTAL energies, indicating overall favorable association under the modeled conditions. The LRRK2–TMZ complex exhibited the most favorable predicted binding (−18.45 kcal·mol^{-1}), followed by Dectin-1–TMZ (−12.49 kcal·mol^{-1}), with α-synuclein–TMZ showing the weakest binding (−6.35 kcal·mol^{-1}). This rank order mirrors trends from docking scores and MD pose stability analyses, lending cross-method support to the relative interaction strengths.

In Dectin-1–TMZ complex, binding is driven by a combination of favorable van der Waals (VDWAALS, −18.63 kcal·mol^{-1}) and Coulombic (electrostatic-electrostatic interaction [EEL], −15.76 kcal·mol^{-1}) interactions formed within the carbohydrate-recognition groove (Supplementary Fig. S2a and Table 2). These favorable gas-phaseinteraction energy terms [GGAS] = −34.39 kcal·mol^{-1}) are partially offset by desolation penalties when transferring TMZ into the pocket (solvation free energy [GSOLV] = + 21.90 kcal·mol^{-1}), yielding a net moderate ΔG_bind. This balance is consistent with the hydrogen-bonding network observed in docking (Asp158, Asn159, and Lys128) and its partial persistence during MD.

The strongest binder by MM-PBSA for LRRK2–TMZ complex shows substantially larger van der Waals stabilization (−31.34 kcal·mol^{-1}) relative to the other systems, reflecting deeper or better-complemented shape complementarity in the kinase pocket. Electrostatics (EEL = −10.83 kcal·mol^{-1}) are modestly favorable, while polar desolation (generalized Born solvation energy [EGB] = + 28.45 kcal·mol^{-1}) and nonpolar solvation (ESURF = −4.74 kcal·mol^{-1}) together yield GSOLV = + 23.72 kcal·mol^{-1} (Figures S3B and Table 2). The resulting TOTAL (−18.45 kcal·mol^{-1}) indicates that hydrophobic/polarizable packing is the dominant stabilizing factor, which is consistent with MD analyses showing persistent interactions with Leu1161, Ala1176, and supporting hydrogen bonding to Lys1034.

α-Synuclein–TMZ system differs markedly in that gas-phase electrostatics are strongly unfavorable (EEL = + 20.44 kcal·mol^{-1}), which is likely reflecting suboptimal charge complementarity and solvent exposure in the shallow fibril surface site identified by docking. Solvation partially compensates (EGB = −11.34 kcal·mol^{-1}; ESURF = −2.06 kcal·mol^{-1}; GSOLV = −13.40 kcal·mol^{-1}), and modest van der Waals stabilization (−13.40 kcal·mol^{-1}) brings the TOTAL to −6.35 kcal·mol^{-1} (Supplementary Figs. S2c and Table 2). The weak net binding, combined with the rapid loss of stable hydrogen bonds observed in MD, suggests that TMZ associates only transiently with this fibrillar surface, which is in agreement with the modest docking score and high local flexibility seen in the RMSF analysis.

To elucidate the key residue-level contributions to the binding affinity of each complex, MM/Generalized Born Surface Area (GBSA) energy decomposition was performed, focusing on van der Waals, electrostatic, polar solvation, and nonpolar solvation components. Among Dectin-1 residues, Lys128, Lys161, Glu162, and Glu243 exhibited the highest stabilizing contributions, with total energies of −2.41, −0.64, + 0.75, and +0.08 kcal/mol, respectively. Lys128 and Lys161 were mainly stabilized by van der Waals (−2.10 and −0.69 kcal/mol) and electrostatic interactions (−1.67 and +0.07 kcal/mol), while Glu162 and Glu243 displayed significant electrostatic repulsions compensated by polar solvation energies (5.04 and 0.76 kcal/mol). The ligand–residue composite term (TMZ) had a pronounced total energy of −8.41 kcal/mol, suggesting a major role in ligand stabilization (Supplementary Figs. S3a and S3b).

In LRRK2, residues Lys1034 (0.53 kcal/mol), Lys1055 (−3.19 kcal/mol), Asp1112 (1.58 kcal/mol), and Asp1177 (1.32 kcal/mol) emerged as key contributors. Lys1055 displayed a strong electrostatic attraction (−4.61 kcal/mol) counterbalanced by polar solvation (2.26 kcal/mol). Asp1177 exhibited a positive polar solvation term (3.28 kcal/mol) that overcame its unfavorable van der Waals interactions (−0.84 kcal/mol). The ligand composite term (TMZ) contributed significantly with a total of −11.01 kcal/mol, the strongest interaction among all complexes (Supplementary Figs. S3c and S3d).

In α-syn, residues Lys58 (0.10 kcal/mol) and Glu61 (−0.005 kcal/mol) were dominant contributors, largely influenced by opposing electrostatic (11.01 and −12.03 kcal/mol) and polar solvation (−10.44 and +12.23 kcal/mol) terms. Glu57 (−0.038 kcal/mol) and Thr75 (0.018 kcal/mol) showed modest stabilization. The ligand composite term (−4.28 kcal/mol) indicated weaker global binding relative to LRRK2 but comparable to Dectin-1 (Supplementary Figs. S3e and S3f).

Discussion

Ulcerative colitis (UC) is a recurrent inflammatory bowel disease marked by mucosal inflammation that starts distally and can spread throughout the colon (Gajendran et al., 2019). This study explores the roles of Dectin-1, LRRK2, and α-syn in UC-associated motor dysfunction and evaluates TMZ's impact on behavioral and physical outcomes in a DSS-induced UC model using BALB/c mice. UC was induced by administering 3% DSS in drinking water over five cycles (7 days DSS, 10

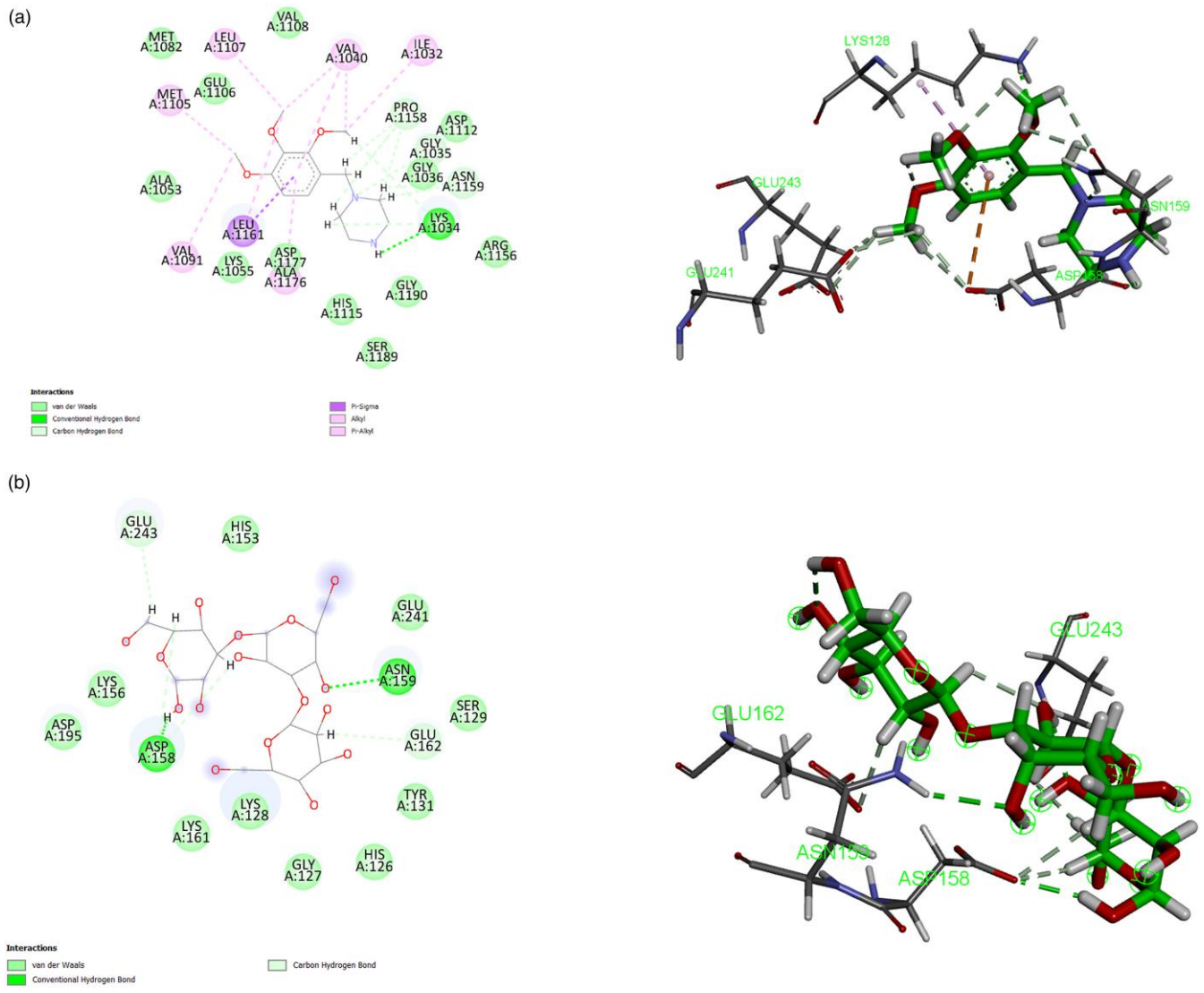

Fig. 20. 2D and 3D Diagrams show the interaction between Trimetazidine (**a**) and Laminarin (**b**) and active sites of the Dectin-1 (2BPH) protein.

days water), effectively reproducing UC features such as significant weight loss, reduced colon length, and elevated fecal occult blood (FOB) and calprotectin levels—hallmarks of DSS-induced colitis, consistent with Zhou et al. (2023), who observed similar effects using 1.3% DSS across three cycles. Fecal calprotectin, a marker of colitis severity and inflammation (Amara et al., 2019; Li et al., 2021*b*; Alkushi et al., 2022), has also been used to predict Crohn's disease relapse after infliximab withdrawal (de Suray et al., 2012). The 3% DSS model showed elevated FOB levels, aligning with Zhou et al. (2019), who examined fecal microbiota transplantation in DSS-induced colitis.

Notably, TMZ administration demonstrated significant therapeutic benefits in DSS-treated mice, including attenuated weight loss and marked reduction in both fecal calprotectin and FOB levels, indicating substantial mitigation of intestinal inflammation. These outcomes underscore TMZ's potential as an effective anti-inflammatory agent for UC management, corroborating reports by Ishida et al. (2022) that identify FOB reduction as an indicator of resolving intestinal inflammation. Collectively, these results highlight TMZ's dual capacity to target both inflammatory and reparative pathways in UC pathogenesis.

The significant upregulation of IFN-γ and NF-κB observed in the DSS-induced UC model supports their well-established roles as central mediators of inflammation in both UC and PD. TMZ administration significantly downregulated both IFN-γ and NF-κB compared to the DSS group, suggesting its potential as a dual-pathway modulator in UC-PD comorbidity. The elevation of IFN-γ aligns with previous reports of its increased levels in the colon of DSS-treated wild-type mice (Ito et al., 2006) and its role in PD-related neuroinflammation, as shown in PD monkey serum, where elevated IFN-γ correlates with glial activation (Barcia et al., 2012). Importantly, TMZ's suppression of IFN-γ is clinically relevant, as this cytokine contributes to both intestinal barrier dysfunction in colitis (Nava et al., 2010) and Levodopa (L-DOPA)-induced dyskinesia in PD (Ferrari et al., 2021). These findings suggest that TMZ may act as an effective immunomodulator by directly targeting pro-inflammatory cytokine networks (Alcalay et al., 2015). Similarly, TMZ significantly inhibited NF-κB activation, which plays a pivotal role in orchestrating inflammatory responses in both UC and PD. Our data confirm the central role of NF-κB in DSS-induced colitis and extend its significance to PD, where its activation in microglia contributes

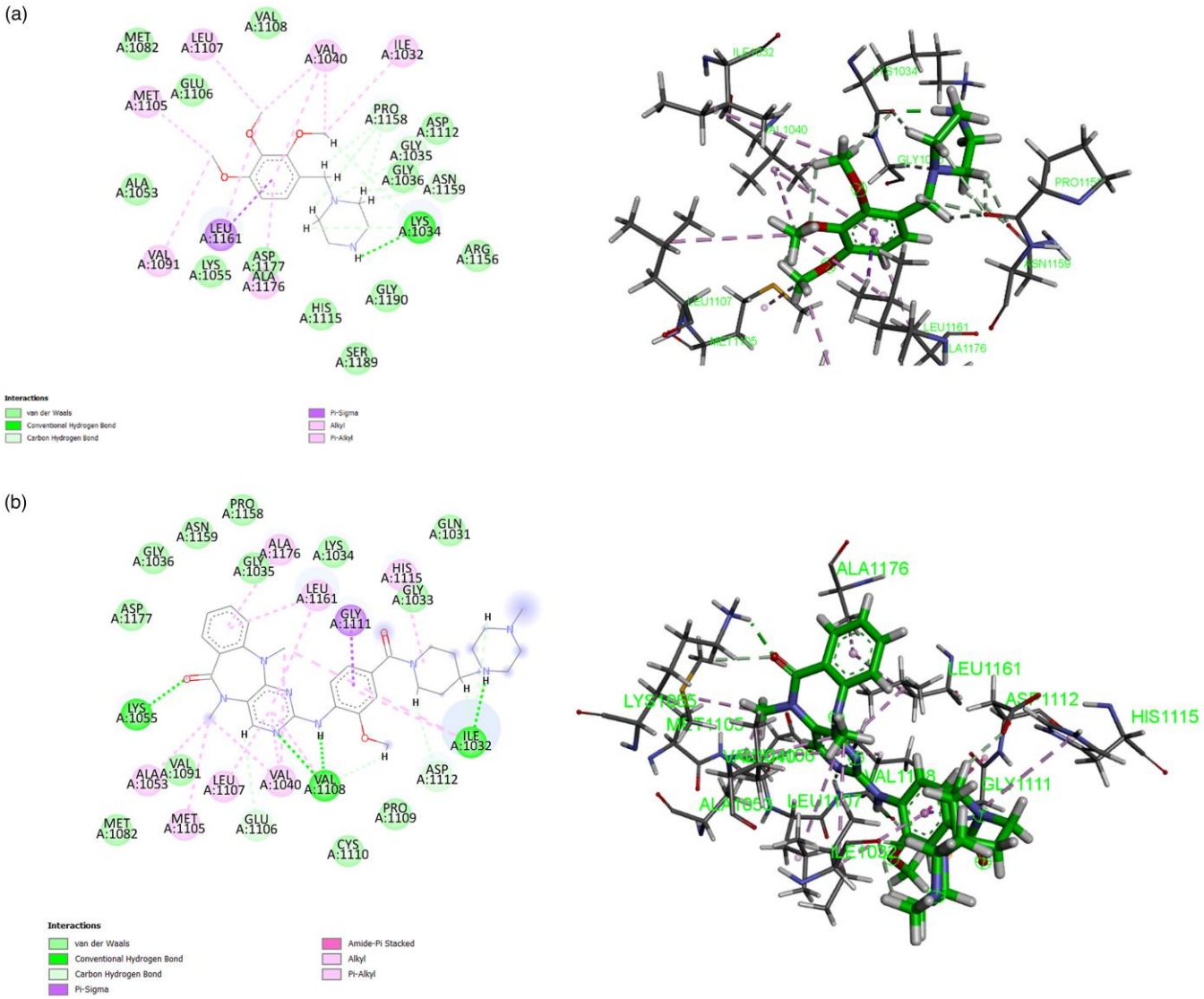

Fig. 21. 2D and 3D diagrams show the interaction between Trimetazidine (**a**) and LRRK2-IN-1 (**b**) and the active sites of LRRK2 (4YZM) protein.

to disease pathology (Zhu et al., 2019). Peterson and Flood (2012) demonstrated that NF-κB activation in microglial cells drives the expression of pro-inflammatory genes, including IKappaB Kinase (IKKβ) and IKKγ, suggesting that NF-κB represents a convergence point for inflammation in both diseases. Therefore, TMZ's inhibition of NF-κB may enhance therapeutic efficacy by disrupting these shared inflammatory cascades.

These molecular findings were jointly supported by histological evidence. H&E staining of colonic tissues from the DSS group revealed severe structural abnormalities, including loss of epithelial architecture, infiltration of inflammatory cells, submucosal edema, and thickening of the colon wall. These changes are consistent with prior reports describing DSS-induced colitis pathology (Kitajima et al., 2000; Erben et al., 2014). Villanacci et al. (2023) similarly reported increased inflammatory marker deposition and extensive fibrosis, particularly in the middle and distal colon. In contrast, colonic tissue from TMZ-treated mice exhibited notable histological improvement, confirming its anti-inflammatory and tissue-protective effects. By suppressing NF-κB activity and lowering IFN-γ levels, TMZ not only reduces inflammation but also promotes mucosal healing and structural recovery. These effects reinforce TMZ's promise as a potential therapeutic agent for UC and potentially for UC-PD comorbidity. Future studies should explore TMZ's precise molecular targets, particularly its interaction with the IKK complex, and evaluate its long-term neuroprotective efficacy in chronic PD models to fully elucidate its therapeutic potential.

Previous studies have linked UC complications to extrapyramidal disorders such as PD, suggesting that UC may contribute to PD pathogenesis (Zhu et al., 2022). PD progression is marked by a substantial loss of dopaminergic neurons in the substantia nigra pars compacta (SNc), primarily involving α-synuclein (αSyn), a key pathological hallmark (Zhu et al., 2022). Chronic low-level gastrointestinal inflammation may trigger PD by facilitating misfolded αSyn transmission to the brain via a compromised blood-brain barrier or the vagus nerve. Garrido-Gil et al. (2018) demonstrated that acute or sub-chronic gut inflammation in mice resulted in early nigrostriatal dopaminergic disruptions, neuronal death, and elevated nigral pro-inflammatory markers. Furthermore, chronic mild gut inflammation induced by 0.3% DSS accelerated motor dysfunction and worsened αSyn pathology in a PD model (Kishimoto et al., 2019).

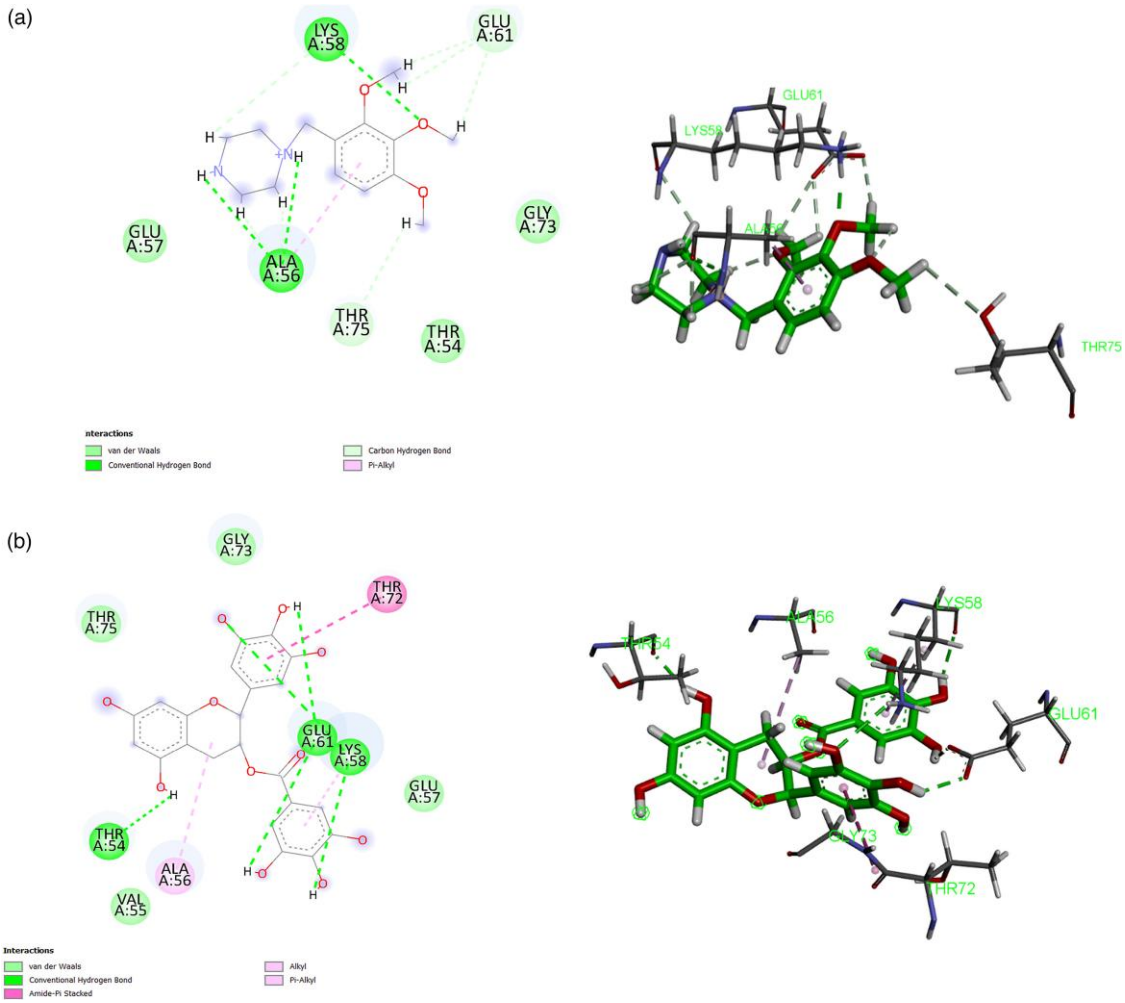

Fig. 22. 2D and 3D diagrams show the interaction between Trimetazidine (**a**) and EGCG (**b**) and the active sites of α-Synuclein (6A6B) protein.

In this study, the rotarod test was used to assess PD-related locomotor impairment in DSS-induced UC-BALB/c mice. DSS administration led to a significant reduction in latency to fall, indicating motor deficits. TMZ treatment significantly improved performance, demonstrating its neuroprotective potential. These results are consistent with previous research using 6-hydroxydopamine (6-OHDA) in PD mouse models, which showed behavioral deficits (Iancu et al., 2005). Supporting evidence also shows that TMZ does not impair motor function in the rotarod test in rodent models of inflammation, pain, and gastric injury (Abdel-Salam & El-Batran, 2005).

Additional PD model studies reported reduced locomotor coordination and balance by the sixth week of subcutaneous rotenone injections, confirmed by rotarod performance deficits (Thong-Asa et al., 2021). Collectively, these findings highlight the rotarod test's effectiveness in detecting PD-related motor impairments and support TMZ's therapeutic potential in alleviating such deficits.

This study identified impairments in exploratory behaviour—specifically reduced center zone entries, rearing, and grooming frequency—in DSS-administered mice, as measured by the OFT. TMZ treatment restored motor activity, supporting its neuroprotective effect. This observation is consistent with prior studies on neurodegenerative diseases where motor deficits stem from α-synuclein pathology and LRRK2-linked autophagic dysfunction (Alcalay et al., 2015; Steger et al., 2017).

The current research emphasizes inflammation-targeted autophagy modulation. TMZ's effects were examined on Dectin-1, LRRK2, *α*Syn, and autophagy markers P62 and LAMP2, uncovering mechanisms by which TMZ mitigates UC-driven inflammatory and neuroinflammatory responses. The study found significant increases in colonic and cerebral *α*Syn expression. This aligns with clinical findings in Inflammatory Bowel Disease (IBD) patients, where *α*Syn aggregation was observed in various parts of the colon (Shannon et al., 2012). Similarly, defective autophagy has been implicated in idiopathic PD due to elevated endogenous *α*Syn and LRRK2 levels (Friedman et al., 2012). However, Prigent et al. (2019) reported increased *α*Syn in Crohn's disease but not in UC, contradicting our findings.

We also observed a marked increase in Dectin-1 expression in the colon and brain; this is consistent with Takagawa et al. (2018), who reported that Dectin-1 overexpression exacerbated inflammatory responses in colitis models. Ding et al. (2022) further demonstrated that elevated Dectin-1 on microglia activates neuroinflammatory pathways. For LRRK2, significant upregulation was found in both colon and brain tissues, echoing Takagawa et al. (2018), who reported its involvement in promoting inflammation in colitis models. Vora and McGovern (2012) noted that LRRK2 deficiency can drive colitis pathogenesis, emphasizing the role of innate immunity. Notably, over 20 LRRK2 mutations have

been associated with autosomal-dominant Parkinsonism (Mata et al., 2006).

TMZ treatment significantly decreased Dectin-1 levels in brain and colon tissues, aligning with Calabresi et al. (2023), who showed Dectin-1's immune role in UC and PD models. Although our findings support TMZ's role in lowering Dectin-1, other researchers, such as Atashrazm et al. (2019), suggest that Dectin-1 should be targeted via autophagy rather than direct anti-inflammatory strategies. Additionally, TMZ reduced LRRK2 levels in the brain and colon, suggesting protective effects via regulation of LRRK2 expression—important for maintaining synaptic integrity and intestinal epithelial health.

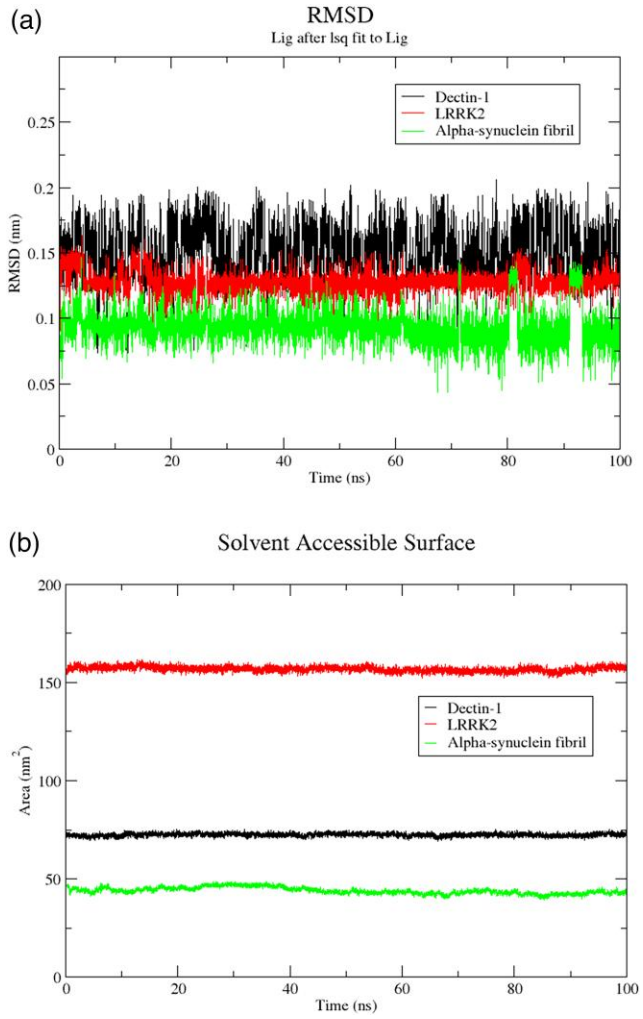

Fig. 23. (**a**) Root mean square deviation (RMSD) profiles of TMZ within the binding cavities of Dectin-1 (PDB ID: 2BPH), LRRK2 (PDB ID: 4YZM), and α-synuclein fibril (PDB ID: 6A6B) over a 100 ns molecular dynamics simulation. (**b**) Solvent-accessible surface area (SASA) plots of the three protein–MZ complexes.

This study found a decline in αSyn levels following TMZ treatment, suggesting that TMZ may mitigate αSyn dysregulation caused by inflammation in UC and PD. While our findings support TMZ's direct effect on αSyn, other studies emphasize the role of autophagy in regulating αSyn levels in neurodegenerative diseases (Zhu et al., 2019), highlighting TMZ's potential as a direct αSyn modulator, which contrasts with the autophagy-centered approach reported in other studies.

Moreover, our study showed that TMZ increased LAMP2 and decreased P62 levels, indicating a restoration of disrupted autophagic processes in UC. However, evidence remains limited on TMZ's direct targeting of these autophagy markers. Several studies recommend selective modulation of autophagy via LRRK2, Dectin-1, and αSyn pathways for optimal outcomes (Daher et al., 2014), suggesting that while TMZ shows promise, it may be most effective as part of a combination therapy targeting multiple mechanisms.

Histologically, H&E staining of mouse brains revealed neuronal loss and abnormal neuronal morphology in the SNc, indicative of neurodegeneration. Immunohistochemistry of colonic tissue in DSS mice also showed disrupted cellular architecture, inflammatory infiltration, edematous submucosa, and increased colon wall thickness. Comparable findings in other models reinforce these observations. Jerzemowska et al. (2014) reported significant loss of TH-positive dopaminergic neurons in the SNc of adult male Wistar rats in a PD model. Similarly, Id2−/− mice exhibited decreased TH-positive fibers in the SNc at 6 months of age, correlating with reduced physical activity and Parkinson's-like 's-like histological changes (Havrda et al., 2013). Kim et al. (2006) also observed significantly higher nigral TH immunoreactivity in older mice compared to younger ones, possibly reflecting reduced dopaminergic activity with age. Overall, these results position TMZ as a promising candidate for addressing both intestinal and neuroinflammatory dysfunction through modulation of immune signaling and autophagy, with implications for the management of UC-PD comorbidity.

This study employed extensive molecular modeling to assess TMZ's binding affinity toward Dectin-1 (PDB ID: 2BPH), LRRK2 (PDB ID: 4YZM), and α-syn (PDB ID: 6A6B). Docking results revealed that TMZ exhibited moderate but consistent binding free energies (ΔG ranging from −5.55 to −6.36 kcal·mol^{-1}), aligning well with experimental and literature data. Notably, TMZ docking poses showed convergence with key residues: Asp158 and Asn159 in Dectin-1, Leu1161 and Ala1176 in LRRK2, and Lys58 in α-synuclein. These residues correspond to known interaction sites for reference ligands such as Laminarin, LRRK2-IN-1, and EGCG, supporting the docking protocol's structural validity. The small ΔG differences between TMZ and known ligands (≤0.54 kcal·mol^{-1}) fall within AutoDock4's expected scoring error margins, reinforcing the hypothesis that TMZ interacts with functionally relevant binding pockets rather than non-specific surfaces. These findings support TMZ's potential as

Table 2. MM-PBSA Binding Free Energy Components for TMZ Complexes (Dectin-1, LRRK2, α-Synuclein).

System	VDWAALS	EEL	EGB	ESURF	GGAS	GSOLV	TOTAL
Dectin-1-TMZ	−18.63 ± 2.27	−15.76 ± 6.04	24.62 ± 6.21	−2.72 ± 0.24	−34.39 ± 6.44	21.90 ± 6.09	**−12.49 ± 2.33**
LRRK2–TMZ	−31.34 ± 2.11	−10.83 ± 4.16	28.45 ± 3.91	−4.74 ± 0.23	−42.17 ± 4.60	23.72 ± 3.90	**−18.45 ± 3.97**
α-Synuclein–TMZ	−13.40 ± 2.97	20.44 ± 10.26	−11.34 ± 9.67	−2.06 ± 0.40	7.05 ± 9.87	−13.40 ± 9.68	**−6.35 ± 2.36**

Values are in kcal·mol^{-1}; average ± SD shown. GGAS = VDWAALS + EEL. GSOLV = EGB + ESURF. TOTAL = GGAS + GSOLV.

a multi-target scaffold relevant to neuroinflammatory and neurodegenerative conditions through its engagement with Dectin-1 and α-synuclein.

Molecular dynamics (MD) simulations over 100 ns further validated TMZ's interaction stability with each target. RMSD and RMSF analyses indicated the highest stability in the LRRK2–TMZ complex, with fluctuations under 0.02 nm, consistent with a tightly packed ATP-binding pocket. In contrast, the α-syn–TMZ complex exhibited higher flexibility, consistent with the fibrillar protein's dynamic surface. Hydrogen-bond analysis confirmed persistent interactions in LRRK2 (notably with Lys1034), while Dectin-1 maintained one–three stable hydrogen bonds via Asp158 and Asn159. α-Synuclein, however, showed a rapid loss of hydrogen bonding, suggesting weaker, nonspecific interactions.

MM-PBSA binding free energy calculations corroborated these trends. The LRRK2–TMZ complex exhibited the most favorable binding energy (−18.45 kcal·mol^{-1}), dominated by van der Waals interactions, typical of well-packed kinase sites. Dectin-1–TMZ showed moderate affinity (−12.49 kcal·mol^{-1}), while α-synuclein–TMZ had the weakest (−6.35 kcal·mol^{-1}), reflecting poor electrostatic compatibility and high solvent exposure. Residue-level energy decomposition revealed strong contributions from Lys1055 and Ala1176 in LRRK2 (hinge-region residues), and from Lys128 and Asp158 in Dectin-1 (carbohydrate-binding groove). In contrast, α-synuclein's contribution was minimal, underlining the challenges in targeting disordered protein surfaces. In conclusion, the molecular docking and MD simulations provide consistent and complementary evidence that TMZ differentially interacts with key UC- and PD-related targets. Its most stable and energetically favorable interactions occur with LRRK2, followed by Dectin-1, with minimal stability in α-synuclein. These findings suggest that TMZ may serve as a valuable scaffold for developing multi-target agents against colonic inflammation and associated neurodegenerative processes.

Conclusion

The significance of this work stems from two observational cores. First, we preliminarily demonstrated the therapeutic potential of TMZ, evidenced by amelioration of colonic inflammation and improvement of motor/behavioral dysfunction, likely through modulation of the Dectin-1, LRRK2, and α-Synuclein pathway. Second, we identified TMZ's influence on autophagy dynamics through modulation of P62 and LAMP2 expression levels. These findings were supported by histological improvements in both brain and colonic tissues. Molecular docking and dynamics simulations further revealed stable binding interactions between TMZ and Dectin-1/LRRK2/α-Synuclein. However, the exact mechanisms through which TMZ influences autophagy and whether these effects confer broader neuroprotection remain unclear. Further research and clinical studies are needed to validate our findings and establish the long-term safety and efficacy of TMZ as a potential therapy for PD associated with UC. In summary, this study highlights a potential novel pathway in inflammatory bowel disease-associated motor dysfunction and suggests TMZ as a candidate for future experimental and preclinical research.

Study Limitation

The authors acknowledge that while this study characterizes TMZ's effects on inflammatory and autophagy pathways, several significant aspects require further investigation. The potential antioxidant properties of TMZ, including its effects on Superoxide dismutase SOD and reduced glutathione (GSH) levels, have yet to be thoroughly evaluated. Moreover, alterations in gut microbiota composition through 16S rRNA sequencing and metagenomic analysis were not assessed. These two aspects play critical roles in UC pathogenesis and neuroinflammation. The exclusive use of male BALB/c mice imposes limitations on the generalizability of the findings, given the established literature documenting sex differences in colitis and neurodegenerative responses. Finally, while the acute DSS model provided valuable insights, chronic colitis models with extended TMZ treatment provide a more comprehensive evaluation of its therapeutic potential for human UC progression.

Availability of Data and Materials Statement

Data supporting the results reported in this manuscript are included in this article. The raw data supporting the conclusions of this article will be made available by the authors without any undue reservation.

Supplementary Material

To view supplementary material for this article, please visit https://doi.org/10.1093/mam/ozaf118.

Acknowledgments

The authors acknowledge the Ain Shams University and Port Said University for their unwavering support during the course of the research.

Author Contributions Statement

Conceptualization, S.H.M., D.I.M. and H.H.A.N; methodology, S.M.H.A., A.N.S., O.A.E., D.A.A.E., E.R.S., T.M.I.A., H.A.A., F.O.A. and D.I.M.; software A.M.E., S.F.E., A.E., S.M.H.A., and S.H.M.; validation. D.I.M., A.N.S., D.A.A.E., F.O.A., H.A.A., S.H.M., T.M.I.A., S.F.E. and H.H.A.N.; formal analysis, S.H.M., S.M.H.A., A.N.S., D.A.A.E., A.M.E. E.R.S., T.M.I.A., A.E., H.A.A., and H.H.A.N; investigation, O.A.E., A.M.E., A.N.S., E.R.S., S.M.H.A., F.O.A. H.A.A., T.M.I.A., S.F.E., S.H.M., D.I.M., and H.H.A.N.; resources, S.H.M., D.I.M., D.A.A.E., A.M.E. E.R.S; T.M.I.A., O.A.E., S.M.HA., A.N.S., A.E., H.A.A, and H.H.A.N., ; data curation, T.M.I.A., A.N.S., O.A.E., D.A.A.E., E.R.S., and H.H.A.N., ; writing—original draft preparation, O.A.E., A.M.E., A.N.S., E.R.S., S.M.H.A., F.O.A., S.H.M., S.F.E., A.E., H.A.A writing—review and editing, A.M.E., S.F.E., A.E., S.M.H.A., E.R.S., H.A.A., O.A.E., S.F.E., A.N.S., D.I.M., and H.H.A.N., ; visualization, S.M.HA., A.N.S., A.E., S.M.H.A., E.R.S., H.A.A., O.A.E., S.F.E., H.A.A, E.R.S., T.M.I.A and H.H.A.N., ; supervision, D.I.M., S.H.M., and H.H.A.N.; project administration, D.I.M., E.R.S., S.M.H.A, . S.H.M., and H.H.A.N.; funding acquisition, E.R.S., A.N.S., T.M.I.A., S.M.H.A., A.E., A.N.S., and H.H.A.N., All authors have read and agreed to the published version of the manuscript.

Financial Support

The authors declare that financial support was received for the research, authorship, and/or publication of this article. This

research was funded by Princess Nourah bint Abdulrahman University Researchers Supporting Project number (PNURSP2025R110), Princess Nourah bint Abdulrahman University, Riyadh, Saudi Arabia.

Conflicts of Interest

The authors declare that they have no competing interest.

Ethical Standards

The animal study protocol was performed following the local legislation and institutional requirements and approved by the Institutional Review Board (or Ethics Committee) of the Faculty of Medicine, Ain Shams University (protocol code (FMASUMD992022) according to the Committee on Animal Research Ethics (CARE) under the guidelines of the Norwegian National Committee for Research Ethics in Science and Technology (NENT). This research was performed at the Faculty of Medicine, Ain Shams University, Cairo, Egypt.

References

Abdel-Salam OME & El-Batran S (2005). Pharmacological investigation of trimetazidine in models of inflammation, pain and gastric injury in rodents. *Pharmacology* **75**(3), 122–132. https://doi.org/10.1159/000088211

Abdel-Salam OM, Mohammed NA & Sleem AA (2011). The effects of trimetazidine on lipopolysaccharide-induced oxidative stress in mice. *EXCLI journal* 10:162.

AboNahas HH, Darwish AMG, Abd EL-kareem HF, AboNahas YH, Mansour SA, Korra YH, Sayyed RZ, Abdel-Azeem AM, & Saied, EM (2022). Trust your gut: The human gut microbiome in health and disease. In *Microbiome-Gut-Brain Axis: Implications on Health*, RZ Sayyed & M Khan (Eds.), pp. 53–96. Singapore: Springer Nature. https://doi.org/10.1007/978-981-16-1626-6_3

Abuelezz SA, Hendawy N & Magdy Y (2017). Targeting oxidative stress, cytokines and serotonin interactions via indoleamine 2, 3 dioxygenase by coenzyme Q10: Role in suppressing depressive like behavior in rats. *J Neuroimmune Pharmacol* **12**(2), 277–291. https://doi.org/10.1007/s11481-016-9712-7

Alcalay RN, Levy OA, Waters CC, Fahn S, Ford B, Kuo S-H, Mazzoni P, Pauciulo MW, Nichols WC, Gan-Or Z, Rouleau GA, Chung WK, Wolf P, Oliva P, Keutzer J, Marder K & Zhang X (2015). Glucocerebrosidase activity in Parkinson's disease with and without GBA mutations. *Brain* **138**(9), 2648–2658. https://doi.org/10.1093/brain/awv179

Alkushi AG, Elazab ST, Abdelfattah-Hassan A, Mahfouz H, Salem GA, Sheraiba NI, Mohamed EAA, Attia MS, El-Shetry ES, Saleh AA, ElSawy NA & Ibrahim D (2022). Multi-strain-probiotic-loaded nanoparticles reduced colon inflammation and orchestrated the expressions of tight junction, NLRP3 inflammasome, and caspase-1 genes in DSS-induced colitis model. *Pharmaceutics* **14**(6), 1183. https://doi.org/10.3390/pharmaceutics14061183

Alzahrani AR, Mohamed DI, Abo Nahas HH, Alaa El-Din Aly El-Waseef D, Altamimi AS, Youssef IH, Ibrahim IAA, Mohamed SM, Sabry YG, Falemban AH, Elhawary NA, Bamagous GA, Jaremko M & Saied EM (2024). Trimetazidine alleviates bleomycin-induced pulmonary fibrosis by targeting the long noncoding RNA CBR3-AS1-mediated miRNA-29 and resistin-like molecule alpha 1: Deciphering a novel trifecta role of LncRNA CBR3-AS1/miRNA-29/FIZZ1 axis in lung fibrosis. *Drug Des Devel Ther* **18**, 3959–3986. https://doi.org/10.2147/DDDT.S463626

Amara J, Saliba Y, Hajal J, Smayra V, Bakhos J-J, Sayegh R & Fares N (2019). Circadian rhythm disruption aggravates DSS-induced colitis in mice with fecal calprotectin as a marker of colitis severity. *Dig Dis Sci* **64**(11), 3122–3133. https://doi.org/10.1007/s10620-019-05675-7

Atashrazm F, Hammond D, Perera G, Bolliger MF, Matar E, Halliday GM, Schüle B, Lewis SJG, Nichols RJ & Dzamko N (2019). LRRK2-mediated Rab10 phosphorylation in immune cells from Parkinson's disease patients. *Mov Disord* **34**(3), 406–415. https://doi.org/10.1002/mds.27601

Barcia C, Ros CM, Annese V, Gómez A, Ros-Bernal F, Aguado-Llera D, Martínez-Pagán ME, de Pablos V, Fernandez-Villalba E & Herrero MT (2012). IFN-γ signaling, with the synergistic contribution of TNF-α, mediates cell-specific microglial and astroglial activation in experimental models of Parkinson's disease. *Cell Death Dis* **3**(8), e379. https://doi.org/10.1038/cddis.2012.123

Calabresi P, Di Lazzaro G, Marino G, Campanelli F & Ghiglieri V (2023). Advances in understanding the function of alpha-synuclein: Implications for Parkinson's disease. *Brain* **146**(9), 3587–3597. https://doi.org/10.1093/brain/awad150

Chartier S & Duyckaerts C (2018). Is Lewy pathology in the human nervous system chiefly an indicator of neuronal protection or of toxicity? *Cell Tissue Res* **373**(1), 149–160. https://doi.org/10.1007/s00441-018-2854-6

Daher JP, Volpicelli-Daley LA, Blackburn JP, Moehle MS & West AB (2014). Abrogation of α-synuclein-mediated dopaminergic neurodegeneration in LRRK2-deficient rats. *Proc Natl Acad Sci* **111**(25), 9289–9294.

de Suray N, Salleron J, Vernier-Massouille G, Grimaud JC, Bouhnik Y, Laharie D, Dupas J-L, Pillant H, Picon L, Veyrac M, Flamant M, Savoye G, Jian R, De Vos M, Piver E, Mary JY, Colombel J-F & Louis E (2012). P274 Close monitoring of CRP and fecal calprotectin levels to predict relapse in Crohn's disease patients. A subanalysis of the STORI study. *J Crohn's Colitis* **6**(Supplement_1), S118–S119. https://doi.org/10.1016/S1873-9946(12)60294-3

Dézsi CA (2016). Trimetazidine in practice: Review of the clinical and experimental evidence. *Am J Ther* **23**(3), e871–e879. https://doi.org/10.1097/MJT.0000000000000180

Ding Z, Zhong Z, Wang J, Zhang R, Shao J, Li Y, Wu G, Tu H, Yuan W, Sun H & Wang Q (2022). Inhibition of dectin-1 alleviates neuroinflammatory injury by attenuating NLRP3 inflammasome-mediated pyroptosis after intracerebral hemorrhage in mice: Preliminary study results. *J Inflamm Res* **15**, 5917–5933. https://doi.org/10.2147/JIR.S384020

El-Sherbeeny NA & Attia GM (2016). The protective effect of trimetazidine against cisplatin-induced nephrotoxicity in rats. *Can J Physiol Pharmacol* **94**(7), 745–751. https://doi.org/10.1139/cjpp-2015-0472

Erben U, Loddenkemper C, Doerfel K, Spieckermann S, Haller D, Heimesaat MM, Zeitz M, Siegmund B & Kühl AA (2014). A guide to histomorphological evaluation of intestinal inflammation in mouse models. *Int J Clin Exp Pathol* **7**(8), 4557–4576.

Ferrari DP, Bortolanza M & Del Bel EA (2021). Interferon-γ involvement in the neuroinflammation associated with Parkinson's disease and L-DOPA-induced dyskinesia. *Neurotox Res* **39**(3), 705–719. https://doi.org/10.1007/s12640-021-00345-x

Friedman LG, Lachenmayer ML, Wang J, He L, Poulose SM, Komatsu M, Holstein GR & Yue Z (2012). Disrupted autophagy leads to dopaminergic axon and dendrite degeneration and promotes presynaptic accumulation of α-synuclein and LRRK2 in the brain. *J Neurosci* **32**(22), 7585–7593. https://doi.org/10.1523/JNEUROSCI.5809-11.2012

Gajendran M, Loganathan P, Jimenez G, Catinella AP, Ng N, Umapathy C, Ziade N & Hashash JG (2019). A comprehensive review and update on ulcerative colitis. *Dis Mon* **65**(12), 100851. https://doi.org/10.1016/j.disamonth.2019.02.004

Garrido-Gil P, Rodriguez-Perez AI, Dominguez-Meijide A, Guerra MJ & Labandeira-Garcia JL (2018). Bidirectional neural interaction between central dopaminergic and gut lesions in Parkinson's disease models. *Mol Neurobiol* **55**(9), 7297–7316. https://doi.org/10.1007/s12035-018-0937-8

Glezer, M. G., Vygodin, V. A., & ODA investigators. (2018). Anti-anginal effectiveness and tolerability of trimetazidine modified

release 80 mg once daily in stable angina patients in real-world practice. *Adv Ther*, **35**(9), 1368–1377. https://doi.org/10.1007/s12325-018-0756-3

Günther C, Rothhammer V, Karow M, Neurath MF & Winner B (2021). The gut-brain axis in inflammatory bowel disease: Current and future perspectives. *Int J Mol Sci* **22**, 8870. https://doi.org/10.3390/ijms22168870

Habib MZ, Tadros MG, Abd-Alkhalek HA, Mohamad MI, Eid DM, Hassan FE, Elhelaly H, Faramawy YE & Aboul-Fotouh S (2022). Harmine prevents 3 3-nitropropionic acid-induced neurotoxicity in rats via enhancing NRF2-mediated signaling: Involvement of p21 and AMPK. *Eur J Pharmacol* **927**, 175046. https://doi.org/10.1016/j.ejphar.2022.175046

Havrda MC, Paolella BR, Ward NM & Holroyd KB (2013). Behavioral abnormalities and Parkinson's-like histological changes resulting from Id2 inactivation in mice. *Dis Model Mech* **6**(3), 819–827. https://doi.org/10.1242/dmm.010041

Huang J, Rauscher S, Nawrocki G, Ran T, Feig M, de Groot BL, Grubmüller H & MacKerell AD (2017). CHARMM36m: An improved force field for folded and intrinsically disordered proteins. *Nat Methods* **14**(1), 71–73. https://doi.org/10.1038/nmeth.4067

Huynh KK, Eskelinen E-L, Scott CC, Malevanets A, Saftig P & Grinstein S (2007). LAMP proteins are required for the fusion of lysosomes with phagosomes. *EMBO J* **26**(2), 313–324. https://doi.org/10.1038/sj.emboj.7601511

Iancu R, Mohapel P, Brundin P & Paul G (2005). Behavioral characterization of a unilateral 6-OHDA-lesion model of Parkinson's disease in mice. *Behav Brain Res* **162**(1), 1–10. https://doi.org/10.1016/j.bbr.2005.02.023

Ishida N, Kaneko M, Asai Y, Miyazu T, Tamura S, Tani S, Yamade M, Iwaizumi M, Hamaya Y, Osawa S, Furuta T & Sugimoto K (2022). Effect of disease duration on fecal biomarkers in ulcerative colitis: A prospective cohort study. *BMC Gastroenterol* **22**(1), 420. https://doi.org/10.1186/s12876-022-02502-8

Ito R, Shin-Ya M, Kishida T, Urano A, Takada R, Sakagami J, Imanishi J, Kita M, Ueda Y, Iwakura Y, Kataoka K, Okanoue T & Mazda O (2006). Interferon-gamma is causatively involved in experimental inflammatory bowel disease in mice. *Clin Exp Immunol* **146**(2), 330–338. https://doi.org/10.1111/j.1365-2249.2006.03214.x

Jejurikar BL & Rohane SH (2021). Drug designing in discovery studio. *Asian J Res Chem* **14**(2), 135–138. https://doi.org/10.5958/0974-4150.2021.00025.0

Jerzemowska G, Plucińska K, Kuśmierczak M, Myślińska D & Orzeł-Gryglewska J (2014). Locomotor response to novelty correlates with differences in the number and morphology of hypothalamic tyrosine hydroxylase-positive cells in rats. *Brain Res Bull* **101**, 26–36. https://doi.org/10.1016/j.brainresbull.2013.12.009

Johansen T & Lamark T (2011). Selective autophagy mediated by autophagic adapter proteins. *Autophagy* **7**(3), 279–296. https://doi.org/10.4161/auto.7.3.14487

Kaur A & Goggolidou P (2020). Ulcerative colitis: Understanding its cellular pathology could provide insights into novel therapies. *J Inflamm (Lond)* **17**, 15. https://doi.org/10.1186/s12950-020-00246-4

Kayal M & Shah S (2020). Ulcerative colitis: Current and emerging treatment strategies. *J Clin Med* **9**(1), 94. https://doi.org/10.3390/jcm9010094

Kim ST, Choi JH, Kim D & Hwang O (2006). Increases in TH immunoreactivity, neuromelanin, and degeneration in the substantia nigra of middle-aged mice. *Neurosci Lett* **396**(3), 263–268. https://doi.org/10.1016/j.neulet.2005.11.053

Kishimoto T, Hagi K, Nitta M, Kane JM & Correll CU (2019). Long-term effectiveness of oral second-generation antipsychotics in patients with schizophrenia and related disorders: A systematic review and meta-analysis of direct head-to-head comparisons. *World Psychiatry* **18**(2), 208–224. https://doi.org/10.1002/wps.20632

Kitajima S, Takuma S & Morimoto M (2000). Histological analysis of murine colitis induced by dextran sulfate sodium of different molecular weights. *Exp Anim* **49**(1), 9–15. https://doi.org/10.1538/expanim.49.9

Kornelsen J, Witges K, Labus J, Mayer EA & Bernstein CN (2021). Brain structure and function changes in ulcerative colitis. *Neuroimage Rep* **1**(4), 100064. https://doi.org/10.1016/j.ynirp.2021.100064

Lang AE & Lozano AM (1998). Parkinson's disease. Second of two parts. *N Engl J Med* **339**(16), 1130–1143. https://doi.org/10.1056/NEJM199810153391607

Langer V, Vivi E, Regensburger D, Winkler TH, Waldner MJ, Rath T, Schmid B, Skottke L, Lee S, Jeon NL, Wohlfahrt T, Kramer V, Tripal P, Schumann M, Kersting S, Handtrack C, Geppert CI, Suchowski K, Adams RH, Becker C, Ramming A, Naschberger E, Britzen-Laurent N & Stürzl M (2019). IFN-γ drives inflammatory bowel disease pathogenesis through VE-cadherin-directed vascular barrier disruption. *J Clin Invest* **129**(11), 4691–4707. https://doi.org/10.1172/JCI124884

Li H, Chen X, Liu J, Chen M, Huang M, Huang G, Chen X, Du Q, Su J & Lin R (2021*a*). Ethanol extract of *Centella asiatica* alleviated dextran sulfate sodium-induced colitis: Restoration on mucosa barrier and gut microbiota homeostasis. *J Ethnopharmacol* **267**, 113445. https://doi.org/10.1016/j.jep.2020.113445

Li Y, Hintze KJ & Ward RE (2021*b*). Effect of supplemental prebiotics, probiotics, and bioactive proteins on the microbiome composition and fecal calprotectin in C57BL6/j mice. *Biochimie* **185**, 43–52. https://doi.org/10.1016/j.biochi.2021.02.010

Liu H, Dai C, Fan Y, Guo B, Ren K, Sun T & Wang W (2017). From autophagy to mitophagy: The roles of P62 in neurodegenerative diseases. *J Bioenerg Biomembr* **49**(5), 413–422. https://doi.org/10.1007/s10863-017-9727-7

Luo X, Zhong Z, Chong A, Zhang W & Wu X (2021). Function and mechanism of trimetazidine in myocardial infarction-induced myocardial energy metabolism disorder through the SIRT1–AMPK pathway. *Front Physiol* **12**, 645041. https://doi.org/10.3389/fphys.2021.645041

Mata IF, Wedemeyer WJ, Farrer MJ, Taylor JP & Gallo KA (2006). LRRK2 in Parkinson's disease: Protein domains and functional insights. *Trends Neurosci* **29**(5), 286–293. https://doi.org/10.1016/j.tins.2006.03.006

Mohamed DI, Abo Nahas HH, Elshaer AM, El-Waseef DAE-DA, El-Kharashi OA, Mohamed SM, Sabry YG, Almaimani RA, Almasmoum HA & Altamimi AS (2023). Unveiling the interplay between NSAID-induced dysbiosis and autoimmune liver disease in children: Insights into the hidden gateway to autism Spectrum disorders. Evidence from ex vivo, in vivo, and clinical studies. *Front Cell Neurosci* **17**, 1268126. https://doi.org/10.3389/fncel.2023.1268126

Mohamed DI, Alaa El-Din Aly El-Waseef D, Nabih ES, El-Kharashi OA, Abd El-Kareem HF, Abo Nahas HH, Abdel-Wahab BA, Helmy YA, Alshawwa SZ & Saied EM (2022). Acetylsalicylic acid suppresses alcoholism-induced cognitive impairment associated with atorvastatin intake by targeting cerebral miRNA155 and NLRP3: In vivo and in silico study. *Pharmaceutics* **14**(3), 529. https://doi.org/10.3390/pharmaceutics14030529

Morris GM, Goodsell DS, Halliday RS, Huey R, Hart WE, Belew RK & Olson AJ (1998). Automated docking using a Lamarckian genetic algorithm and an empirical binding free energy function. *J Comput Chem* **19**(14), 1639–1662. https://doi.org/10.1002/(SICI)1096-987X(19981115)19:14<1639::AID-JCC10>3.0.CO;2-B

Moscat J & Diaz-Meco MT (2009). P62 at the crossroads of autophagy, apoptosis, and cancer. *Cell* **137**(6), 1001–1004. https://doi.org/10.1016/j.cell.2009.05.023

Nava P, Koch S, Laukoetter MG, Lee WY, Kolegraff K, Capaldo CT, Beeman N, Addis C, Gerner-Smidt K, Neumaier I, Skerra A, Li L, Parkos CA & Nusrat A (2010). Interferon-gamma regulates intestinal epithelial homeostasis through converging beta-catenin signaling pathways. *Immunity* **32**(3), 392–402. https://doi.org/10.1016/j.immuni.2010.03.001

O'Hara DM, Pawar G, Kalia SK & Kalia LV (2020). LRRK2 and α-synuclein: Distinct or synergistic players in Parkinson's disease? *Front Neurosci* **14**, 577. https://doi.org/10.3389/fnins.2020.00577

Okayasu I, Hatakeyama S, Yamada M, Ohkusa T, Inagaki Y & Nakaya R (1990). A novel method in the induction of reliable experimental acute and chronic ulcerative colitis in mice. *Gastroenterology* **98**(3), 694–702. https://doi.org/10.1016/0016-5085(90)90290-h

Panagiotakopoulou V, Ivanyuk D, De Cicco S, Haq W, Arsić A, Yu C, Messelodi D, Oldrati M, Schöndorf DC, Perez M-J, Cassatella RP, Jakobi M, Schneiderhan-Marra N, Gasser T, Nikić-Spiegel I & Deleidi M (2020). Interferon-γ signaling synergizes with LRRK2 in neurons and microglia derived from human induced pluripotent stem cells. *Nat Commun* **11**(1), 5163. https://doi.org/10.1038/s41467-020-18755-4

Peterson LJ & Flood PM (2012). Oxidative stress and microglial cells in Parkinson's disease. *Mediators Inflamm* **2012**, 401264. https://doi.org/10.1155/2012/401264

Prigent A, Lionnet A, Durieu E, Chapelet G, Bourreille A, Neunlist M, Rolli-Derkinderen M & Derkinderen P (2019). Enteric alpha-synuclein expression is increased in Crohn's disease. *Acta Neuropathol* **137**(2), 359–361. https://doi.org/10.1007/s00401-018-1943-7

Safarpour D, Sharzehi K & Pfeiffer RF (2022). Gastrointestinal dysfunction in Parkinson's disease. *Drugs* **82**(2), 169–197. https://doi.org/10.1007/s40265-021-01664-1

Santos-Martins D, Forli S, Ramos MJ & Olson AJ (2014). AutoDock4Zn: An improved AutoDock force field for small-molecule docking to zinc metalloproteins. *J Chem Inf Model* **54**(8), 2371–2379. https://doi.org/10.1021/ci500209e

Seibenhener ML & Wooten MC (2015). Use the Open Field Maze to measure locomotor and anxiety-like behavior in mice. *J Vis Exp* **96**, e52434. https://doi.org/10.3791/52434

Shahmoradian SH, Lewis AJ, Genoud C, Hench J, Moors TE, Navarro PP, Castaño-Díez D, Schweighauser G, Graff-Meyer A, Goldie KN, Sütterlin R, Huisman E, Ingrassia A, Gier Y, Rozemuller AJM, Wang J, Paepe A, Erny J, Staempfli A, Hoernschemeyer J, Großerüschkamp F, Niedieker D, El-Mashtoly SF, Quadri M, Van IJcken WFJ, Bonifati V, Gerwert K, Bohrmann B, Frank S, Britschgi M, Stahlberg H, Van de Berg WDJ & Lauer ME (2019). Lewy pathology in Parkinson's disease consists of crowded organelles and lipid membranes. *Nat Neurosci* **22**(7), 1099–1109. https://doi.org/10.1038/s41593-019-0423-2

Shannon KM, Keshavarzian A, Mutlu E, Dodiya HB, Daian D, Jaglin JA & Kordower JH (2012). Alpha-synuclein in colonic submucosa in early untreated Parkinson's disease. *Mov Disord* **27**(6), 709–715. https://doi.org/10.1002/mds.23838

Steger M, Diez F, Dhekne HS, Lis P, Nirujogi RS, Karayel O, Tonelli F, Martinez TN, Lorentzen E, Pfeffer SR, Alessi DR & Mann M (2017). Systematic proteomic analysis of LRRK2-mediated Rab GTPase phosphorylation establishes a connection to ciliogenesis. *eLife* **6**, e31012. https://doi.org/10.7554/eLife.31012

Takagawa T, Kitani A, Fuss I, Levine B, Brant SR, Peter I, Tajima M, Nakamura S & Strober W (2018). An increase in LRRK2 suppresses autophagy and enhances Dectin-1-induced immunity in a mouse model of colitis. *Sci Transl Med* **10**(444), eaan8162. https://doi.org/10.1126/scitranslmed.aan8162

Thong-Asa W, Jedsadavitayakol S & Jutarattananon S (2021). Benefits of betanin in rotenone-induced Parkinson mice. *Metab Brain Dis* **36**(8), 2567–2577. https://doi.org/10.1007/s11011-021-00826-0

Van Der Spoel D, Lindahl E, Hess B, Groenhof G, Mark AE & Berendsen HJC (2005). GROMACS: Fast, flexible, and free. *J Comput Chem* **26**(16), 1701–1718. https://doi.org/10.1002/jcc.20291

Vanommeslaeghe K, Hatcher E, Acharya C, Kundu S, Zhong S, Shim J, Darian E, Guvench O, Lopes P, Vorobyov I & Mackerell AD (2010). CHARMM general force field: A force field for drug-like molecules compatible with the CHARMM all-atom additive biological force fields. *J Comput Chem* **31**(4), 671–690. https://doi.org/10.1002/jcc.21367

Villanacci V, Del Sordo R, Parigi TL, Leoncini G & Bassotti G (2023). Inflammatory bowel diseases: Does one histological score fit all? *Diagnostics (Basel, Switzerland)* **13**(12), 2112. https://doi.org/10.3390/diagnostics13122112

Villarán RF, Espinosa-Oliva AM, Sarmiento M, De Pablos RM, Argüelles S, Delgado-Cortés MJ, Sobrino V, Van Rooijen N, Venero JL, Herrera AJ, Cano J & Machado A (2010). Ulcerative colitis exacerbates lipopolysaccharide-induced damage to the nigral dopaminergic system: A potential risk factor in Parkinson's disease. *J Neurochem* **114**(6), 1687–1700. https://doi.org/10.1111/j.1471-4159.2010.06879.x

Vora P & McGovern DPB (2012). LRRK2 as a negative regulator of NFAT: Implications for the pathogenesis of inflammatory bowel disease. *Expert Rev Clin Immunol* **8**(3), 227–229. https://doi.org/10.1586/eci.12.11

Warnecke T, Schäfer K-H, Claus I, Del Tredici K & Jost WH (2022). Gastrointestinal involvement in Parkinson's disease: Pathophysiology, diagnosis, and management. *Npj Parkinson's Disease* **8**(1), 1–13. https://doi.org/10.1038/s41531-022-00295-x

Xie J, Guo L, Ruan Y, Zhu H, Wang L, Zhou L, Yun X & Gu J (2010). Laminarin-mediated targeting to dectin-1 enhances antigen-specific immune responses. *Biochem Biophys Res Commun* **391**(1), 958–962. https://doi.org/10.1016/j.bbrc.2009.11.173

Xu Y, Zhang Y, Quan Z, Wong W, Guo J, Zhang R, Yang Q, Dai R, McGeer PL & Qing H (2016). Epigallocatechin gallate (EGCG) inhibits alpha-synuclein aggregation: A potential agent for Parkinson's disease. *Neurochem Res* **41**(10), 2788–2796. https://doi.org/10.1007/s11064-016-1995-9

Zhang C & Cuervo AM (2008). Restoration of chaperone-mediated autophagy in aging liver improves cellular maintenance and hepatic function. *Nat Med* **14**(9), 959–965. https://doi.org/10.1038/nm.1851

Zhou J, Zhou Z, Ji P, Ma M, Guo J & Jiang S (2019). Effect of fecal microbiota transplantation on experimental colitis in mice. *Exp Ther Med* **17**(4), 2581–2586. https://doi.org/10.3892/etm.2019.7263

Zhou Y, Ji G, Yang X, Chen Z & Zhou L (2023). Behavioral abnormalities in C57BL/6 mice with chronic ulcerative colitis induced by DSS. *BMC Gastroenterol* **23**(1), 84. https://doi.org/10.1186/s12876-023-02718-2

Zhu F, Li C, Gong J, Zhu W, Gu L & Li N (2019). The risk of Parkinson's in inflammatory bowel disease: A systematic review and meta-analysis. *Dig Liver Dis* **51**(1), 38–42. https://doi.org/10.1016/j.dld.2018.09.017

Zhu Y, Yuan M, Liu Y, Yang F, Chen W-Z, Xu Z-Z, Xiang Z-B & Xu R-S (2022). Association between inflammatory bowel diseases and Parkinson's disease: Systematic review and meta-analysis. *Neural Regen Res* **17**(2), 344–353. https://doi.org/10.4103/1673-5374.317981